Stretchable and Transparent Biointerface Using Cell-Sheet–Graphene Hybrid for Electrophysiology and Therapy of Skeletal Muscle

Seok Joo Kim, Kyoung Won Cho, Hye Rim Cho, Liu Wang, Sung Young Park, Seung Eun Lee, Taeghwan Hyeon, Nanshu Lu, Seung Hong Choi, and Dae-Hyeong Kim**

Implantable electronic devices for recording electrophysiological signals and for stimulating muscles and nerves have been widely used throughout clinical medicine. Mechanical mismatch between conventional rigid biomedical devices and soft curvilinear tissues, however, has frequently resulted in a low signal to noise ratio and/or mechanical fatigue and scarring. Multifunctionality ranging from various sensing modalities to therapeutic functions is another important goal for implantable biomedical devices. Here, a stretchable and transparent medical device using a cell-sheet–graphene hybrid is reported, which can be implanted to form a high quality biotic/abiotic interface. The hybrid is composed of a sheet of C2C12 myoblasts on buckled, mesh-patterned graphene electrodes. The graphene electrodes monitor and actuate the C2C12 myoblasts in vitro, serving as a smart cell culture substrate that controls their aligned proliferation and differentiation. This stretchable and transparent cell-sheet–graphene hybrid can be transplanted onto the target muscle tissue, to record electromyographical signals, and stimulate implanted sites electrically and/or optically in vivo. Additional cellular therapeutic effect of the cell-sheet–graphene hybrid is obtained by integrated myobalst cell sheets. Any immune responses within implanted muscle tissues are not observed. This multifunctional device provides many new opportunities in the emerging field of soft bioelectronics.

1. Introduction

The measurement of electrophysiological signals from muscles and/or neural tissues is important in the diagnosis of many motor neuron dysfunctions.[1] Continuous monitoring of electromyograms (EMGs), for example, is a basic procedure in treating a variety of neuromuscular disorders including Duchenne muscular dystrophy,[2] spinal muscular atrophy,[3] and Parkinson's disease.[4] Immediate feedback therapeutic actuations, such as electrical stimulation[5,6] and/or drug delivery,[7–9] for relieving those symptoms are commonly accompanied. Although implantable devices play a critical role in the diagnosis and therapy of these neuromuscular disorders, those used in the past were bulky and mechanically rigid. The mechanical mismatch between conventional rigid devices[10] and soft tissues[11,12] with curved shapes has caused nonconformal contacts/interfaces, a low signal to noise ratio, mechanical fatigue,

S. J. Kim, K. W. Cho, Dr. S. Y. Park, Prof. T. Hyeon, Prof. D.-H. Kim
Center for Nanoparticle Research
Institute for Basic Science (IBS)
Seoul 151-742, Republic of Korea
E-mail: dkim98@snu.ac.kr

S. J. Kim, K. W. Cho, Dr. S. Y. Park, Prof. T. Hyeon, Prof. D.-H. Kim
School of Chemical and Biological Engineering
Institute of Chemical Processes
Seoul National University
Seoul 151-742, Republic of Korea

Dr. H. R. Cho, Prof. S. H. Choi
Center for Nanoparticle Research
Institute for Basic Science (IBS)
Seou 151-742, Republic of Korea
E-mail: verocay@snuh.org

Dr. H. R. Cho, Prof. S. H. Choi
Department of Radiology
Seoul National University College of Medicine
Seoul 110-744, Republic of Korea

L. Wang, Prof. N. Lu
Center for Mechanics of Solids
Structures, and Materials
Department of Aerospace Engineering
and Engineering Mechanics
Texas Materials Institute
University of Texas at Austin
210 E 24th Street, Austin, TX 78712, USA

Dr. S. E. Lee
Center for Neural Science
Brain Science Institute
Korea Institute of Science and Technology
Seoul 136-791, Republic of Korea

DOI: 10.1002/adfm.201504578

and occasionally inflammation arising from local friction as well as scarring.[13] On this account, soft bioelectronics based on flexible/stretchable devices[14–19] has been highlighted as a potential solution to these issues.

Multimodal therapeutic functions are another essential feature that should optimally be integrated within an implantable bioelectronic system. Electrical stimulation on the spinal cord[5] and/or neurons[20] has provided effective therapies for limb paralysis. Electrical fatigue, however, sometimes arises from this method.[21] Optical stimulation at target wound sites has been proposed as an alternative strategy and has shown promise for brain stimulation,[17,22,23] although simultaneous electrophysiological recording from optically stimulated tissues with metal electrodes is challenging owing to spatial misalignment of the light source and nontransparent electrodes. Another conventional therapy is to load drugs onto a device, which is then implanted to deliver the cargo to the target area.[24,25] However, the process of drug-incorporation within implantable devices is complicated and multiple drug reloading is difficult.[26,27] The transplantation of cultured cells is thereby emerging as an alternative therapeutic procedure in many diseases and has shown to be effective for tissue regeneration at wound sites.[28,29] In addition, coating muscle cells onto an implantable device improves the interface between the device and adjacent tissues,[30] moving toward the desired high quality biotic/abiotic interface that would enable efficient stimulation therapy with simultaneous monitoring.

Here, we introduce a stretchable and transparent cell-sheet–graphene hybrid comprised of biocompatible materials.[31–34] The device is composed of a cell-sheet–graphene hybrid, an aligned C2C12 myoblast sheet (≈10 μm)[31] integrated on buckled, Au-doped, and mesh-patterned graphene electrodes (≈5 nm),[32] which is mounted on a submicron-thick polyimide (PI) membrane (≈600 nm)[33] and a soft polydimethylsiloxane (PDMS) substrate (500 μm) (**Figure 1**a).[34] All materials are stable and biocompatible in vivo according to previous reports.[31–34] Chronic immune responses in the long-term implantation study should be observed in the future. Serpentine-shaped, mesh-patterned graphene electrodes (≈50 μm width; Figure S1a, Supporting Information) are used to improve stretchability and softness of the system. The electrodes also monitor and promote proliferation and differentiation of muscle cells in vitro[35,36] as well as serve as an electrical stimulator and electrophysiology sensor in vivo. Au doping on the graphene mesh electrodes allows low impedance and high conductivity.[18,37] The anisotropic buckled structure (Figure 1b) induces cell alignment (Figure 1c) and enhances stretchability and softness (Figure 1d).[38] The cell-sheet–graphene hybrid is comprised of transparent materials and thereby can be transversed by the visible light (Figure 1e,f). The stretched system without buckles and light diffraction/scattering shows

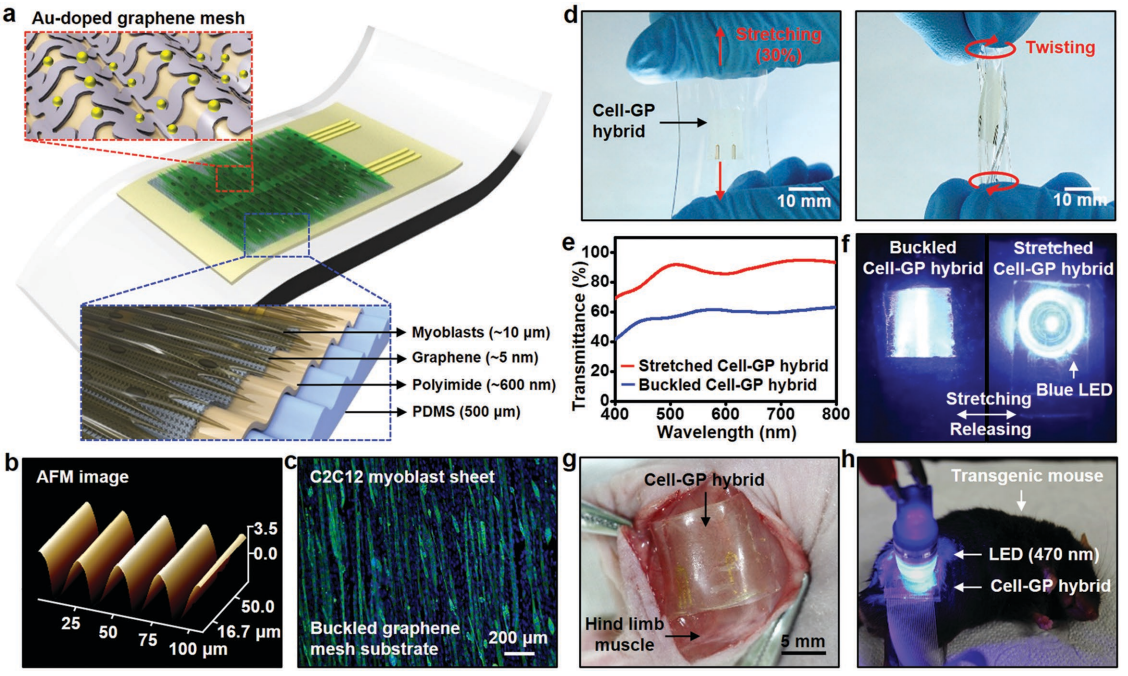

Figure 1. Overview of the architecture of the stretchable and transparent cell-sheet–graphene hybrid (Cell–GP hybrid). a) The hybrid is composed of a C2C12 myoblast sheet (≈10 μm), an ultrathin graphene mesh (≈5 nm), and Au nanomembrane connective electrodes (70 nm), and is mounted on submicron polyimide (≈600 nm) on a PDMS substrate (500 μm) with buckled topology (bottom blue box). The graphene mesh is doped with Au particles (top red box). b) Atomic force microscope image of the buckled graphene mesh. c) C2C12 myoblast sheet on the buckled graphene mesh substrate. Green and blue fluorescences indicate myosin heavy chain and nucleus, respectively. d) Images of the device during uniaxial stretching (left frame) and twisting (right frame). e) Optical transmittance (from 400 to 800 nm of wavelength) and f) photographic images (with 470 nm LED) of the hybrid during buckled and stretched states. g) Implantation of the cell-sheet–graphene hybrid onto target site of a nude mouse in vivo. h) Image of a ChR2-expressing transgenic mouse (*Thy1-ChR2*) and its optogenetic application using the cell-sheet–graphene hybrid device. For optical stimulation, a 470 nm LED is located on top of the transparent cell-sheet–graphene hybrid.

Adv. Funct. Mater. **2016**,
DOI: 10.1002/adfm.201504578

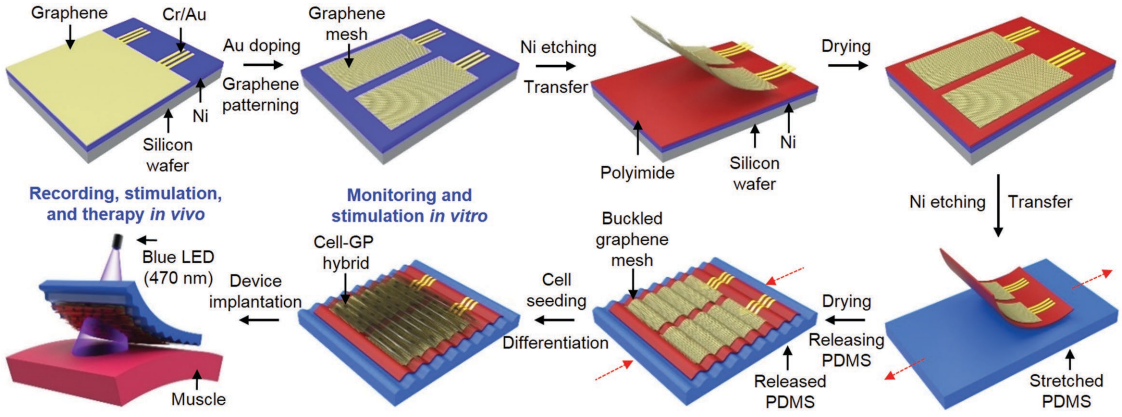

Figure 2. Detailed fabrication process and key applications in vitro and in vivo of the cell-sheet–graphene hybrid.

even better transmittance. Implantation of the system, which includes a cell sheet, enables cell therapy as well as high quality biointerface formation (Figure 1g). Transparency allows the genetically modified muscle tissues underneath the hybrid to be excited by optical stimulation (Figure 1h). We also examine the effectiveness of the integrated system in the diagnosis and therapy of neuromuscular diseases through in vitro and in vivo studies.

2. Results and Discussion

2.1. Fabrication of Buckled and Mesh-Patterned Cell-Sheet–Graphene Hybrid

All fabrication procedures from preparation of the cell-sheet–graphene hybrid device to its in vitro and in vivo applications are graphically illustrated in **Figure 2**. Graphene layers on a copper foil are grown using chemical vapor deposition following protocols described in previous reports.[35,39] A 30 nm Ni layer is deposited onto the Si wafer and, subsequently, 7 nm/70 nm Cr/Au are deposited onto the Ni layer using thermal evaporation. Cr and Au layers are patterned by photolithography and wet etching. Then, the graphene sheet is transferred onto the sample and doped with $AuCl_4$ in nitromethane.[37] The doped sheet is patterned by photolithography and reactive ion etching. The detailed AutoCAD design is shown in Figure S1b in the Supporting Information. The patterned sample is transferred onto the polyimide layer coated on the Ni/Si wafer. The patterned sample on the PI is transferred onto the prestretched (30%) PDMS and dried under 70 °C for 10 min. Then, prestrain of the PDMS is slowly released to form the buckled graphene mesh. Before seeding C2C12 myoblasts, the buckled graphene mesh is sterilized with 70% ethanol for 15 min under UV light and rinsed with phosphate-buffered saline (PBS) solution for 15 min under UV light twice. To prepare cell-sheet–graphene hybrid, C2C12 myoblasts are seeded on the sample with a density of 5×10^4 cells cm^{-2} and cultured by using growth and differentiation media.[35] The formation of high quality biotic/abiotic interface enables the hybrid to electrically/optically stimulate and effectively monitor the electrophysiological characteristics in vitro and in vivo.

2.2. Mechanical Stability of the Buckled and Mesh-Patterned Cell-Sheet–Graphene Hybrid

Figure 3a shows optical microscope images of wavy PI/graphene substrates of two different thicknesses (0.6 μm and 0.35 μm for left and right; images of other wavelengths are shown in Figure S2a in the Supporting Information. By simply controlling the overall thickness between 0.3 and 1.4 μm, uniform buckled structures of different wavelengths can be formed. The wavelength decreases linearly as the PI/graphene thickness is reduced (Figure 3b and Figure S2b, Supporting Information).[40] To determine the optimized wavelength for cell alignment, we cultured C2C12 myoblasts for 3 d on the buckled graphene mesh of different wavelengths. C2C12 myoblasts cultured on the buckled graphene with a 41 μm wavelength show the best alignment (≈98%) as shown in Figure 3c,d; images of other wavelengths are shown in Figure S3 in the Supporting Information. The alignment ratio is determined by the method used in the previous study.[35] The preferred adhesion of proteins and thereby cells to the graphene surface enhances efficiency of the cell culture.[35,41]

The factor that quantifies the softness of bioelectronics is the stretchability. Stretchable devices show superb deformability in bending, twisting, and stretching.[36–44] Minimum electrical hysteresis under deformation is another important advantage of stretchable devices.[16,45] Although both graphene[46] and cells[47,48] are intrinsically soft and stretchy, their stretchabilities may be somewhat limited. The graphene electrodes in the form of a flat sheet, buckled sheet, and buckled mesh are tested under stretching (Figure 3e), compressing (Figure 3f), and bending (Figure 3g) conditions (experiment setups are shown in Figure S4 in the Supporting Information). These deformations mimic the various states of muscular movements (bending, stretching, and compressing). The results in Figure 3e–g support that the buckled graphene mesh is mechanically sustainable under the typical deformation range[49] of muscular movements (25% contraction; 20% stretching). Moreover, the system modulus of the hybrid (61 kPa) is comparable with the elastic modulus of muscle tissue (52 kPa; Figure S5, Supporting Information). Overall, the buckled mesh-patterned electrode shows the best electrical reliability and mechanical stretchability. It is mechanically reliable

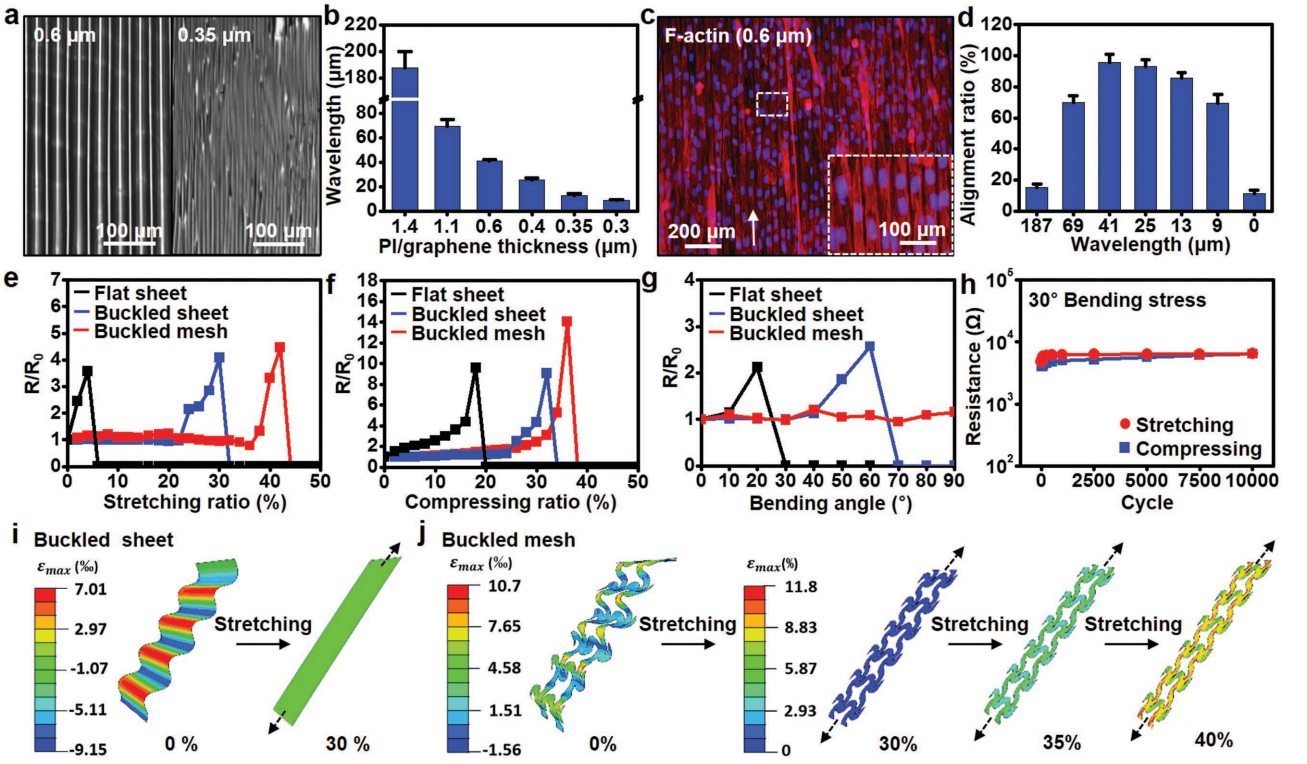

Figure 3. C2C12 myoblast alignments and stretchable characteristics of buckled mesh-patterned graphene electrode. a) Optical microscopic images of buckled mesh-patterned graphene electrodes at different PI/graphene thicknesses. b) Wavelength variation according to PI/graphene thickness. c) Fluorescence microscopic image of aligned C2C12 myoblasts on the buckled mesh-patterned graphene electrode. Actin filaments (F-actin; red) and nuclei (blue) of cells are anisotropically aligned along the buckled topology of the graphene mesh. The bottom right inset shows a magnified view of the white box. d) Alignment ratio of C2C12 myoblasts cultured on topologies of different wavelengths. e–g) Maximal endurance tests of three different samples (including flat sheet, buckled sheet, and buckled mesh) during native muscle-like deformations including e) stretching, f) compressing, and g) bending. h) Fatigue cycling test of the buckled mesh-patterned graphene electrode. i) Strain distributions of a buckled sheet at a relaxed state and with 30% stretching. j) Strain distribution of a buckled mesh at a relaxed state, and with 30%, 35%, and 40% stretching. b,d) Quantitative data are acquired in quadruple ($n = 4$).

even after 10 000 bending cycles (Figure 3h). Details of the mechanics including the induced strain distributions under deformation are analyzed through finite element modeling,[6,50] the results of which support the experimental results (buckled sheet in Figure 3i, and buckled mesh in Figure 3j). The resistance of the graphene mesh begins to increase at the maximum principal strain of 6.17% in modeling (35% stretching) and the graphene mesh is completely fractured at the strain of 11.8% in modeling (40% stretching; extensive finite element modeling (FEM) analysis data are shown in Figure S6 in the Supporting Information).

2.3. Electrochemical Characterization of Au Doping on Buckled Graphene Mesh

Figure 4a shows a schematic illustration of Au doping process on graphene electrodes. Au particles are deposited on graphene electrodes by reducing Au ions, which improves electrode's electrochemical properties. The interface properties such as impedance, capacitance, and cyclic voltammetry (CV) of four different sample electrodes (flat graphene mesh, buckled graphene mesh, Au-doped, and buckled graphene mesh, and flat Au mesh) are measured under PBS solution. Gold is a regularly used material for EMG measuring electrodes. Thus, we implemented a mesh-patterned Au electrode that uses the exactly same device design with our mesh-patterned graphene electrode. Figure 4b,c shows the impedance change and phase response under frequency range between 1 Hz and 1 MHz. Au doping of the buckled graphene mesh significantly decreases its impedance and improves phase responses. Figure 4d illustrates conductance changes, which shows a significantly improved conductance of doped buckled graphene mesh. Electrochemical properties of doped buckled graphene mesh present similar charge transfer characteristics with those of the flat Au mesh.[51] The impedance of materials and the measurement setups bring an effect on the thermal noise, which is an important factor for the signal-to-noise ratio.[52] The electrode-tissue interface noise, however, is also critical in the measurement of EMG signal particularly in the low frequency range (0.5 to 500 Hz)[52] and high amplification condition (>100 times). In Figure 4e, the doped buckled graphene mesh electrode shows larger capacitance than others. This large capacitance minimizes the electrode-tissue interface noise,[53] leading to higher signal-to-noise ratio (Figure S7, Supporting Information), although this effect cannot be seen in low amplification condition (<10 times) due to large thermal and equipment

Adv. Funct. Mater. 2016,
DOI: 10.1002/adfm.201504578

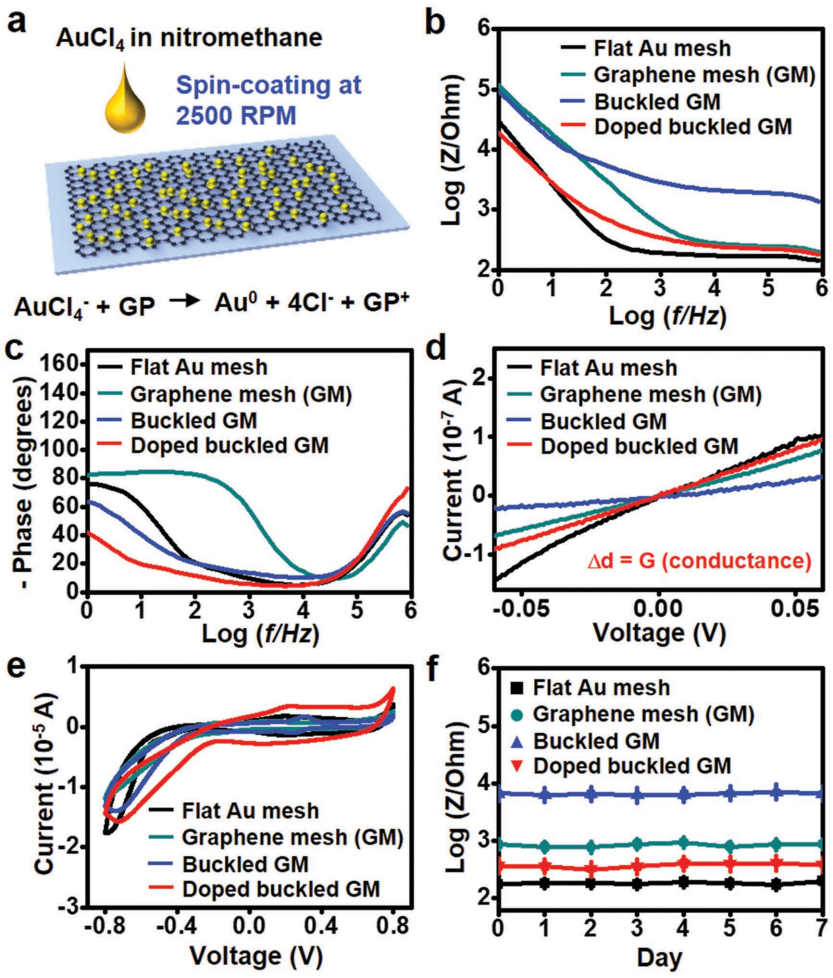

Figure 4. Electrochemical characterization of graphene electrode. a) A schematic image of Au doping process. $AuCl_4$ in nitromethane solvent (20×10^{-3} M) is spin-coated on graphene sheet before graphene patterning. b,c) Measurements of electrochemical impedance spectroscopy with b) impedance and c) phase plots. The curve is measured from 1 Hz to 1 MHz with a bias voltage of 0.01 V. d,e) Measurements of conductance and charge storage capacity by plotting of d) *I–V* curves and e) cyclic voltammograms. The scan rate for measuring the cyclic voltammetry is 100 mV s^{-1}. f) Plot of impedance changes during 7 d at 1 kHz with a bias voltage of 0.01 V. All data of flat Au mesh (black), graphene mesh (GM; dark cyan), buckled graphene mesh (Buckled GM; blue), and Au-doped and buckled graphene mesh (Doped buckled GM; red) are measured in PBS solution at b–e) room temperature and f) growth medium at 37 °C. The area of each sample is 22.8 mm^2.

noises. These results also agree with a previous report.[18] Cyclic voltammetry measurement was repeated for 300 cycles under the same conditions (Figure S8, Supporting Information). This stable electrochemical property and high charge storage capacity are also helpful for effective electrical stimulations in vitro and in vivo. Figure 4f shows impedance changes under growth medium for 7 d to monitor whether materials maintain original electrochemical properties under biofluidic environment.

2.4. Controlled Culture and Monitoring of C2C12 Myoblasts In Vitro

Figure 5a shows a schematic illustration for the controlled culture of C2C12 myoblasts using electrical stimulation via graphene electrodes in vitro. Two different monophasic square wave pulses (high 1 V, 1 Hz; low 0.05 V, 1 Hz) are applied to the direction of myotube elongation (red box in Figure 5a) for 3 d as shown in the timetable of Figure 5b. Elongated and high density culture of myotubes is observed under electrical stimulation using buckled graphene electrodes (10 d culture and 3 d electrical stimulation; Figure 5b), whereas diminished myotube formation is found in the unstimulated culture (Figure 5c). The myotubes are detected and imaged by immunostaining of myosin heavy chains. Although the average area per a myotube increases in all groups (0 V, low, and high) from 7 to 10 d of culture, the increases for electrically stimulated groups are significantly greater than those in the control group (0 V; Figure 5d). Myotube length changes show similar trends (Figure 5e).

Cell proliferation and differentiation change the electrochemical environment of cultured cells.[35,36] These changes can be monitored through impedance measurements by using integrated graphene electrodes. Two mesh-patterned graphene electrodes spaced ≈300 µm apart serve as an impedance sensor, which continuously monitor impedance changes during proliferation and differentiation of skeletal muscle cells controlled by electrical stimulation, as shown in the schematic description in Figure 5f. The impedance during cell proliferation increases since the electrodes are covered with proliferated cells that act as a high resistance barrier to the conductive medium, whereas the impedance during differentiation decreases because of the formation of conducting myotubes (Figure 5g). Figure 5h shows the time-dependent impedance changes (at 0.82 kHz) of myotubes and human dermal fibroblasts (control; hDFBs) during both proliferation and differentiation. The impedance of fibroblasts, however, continuously increases because they do not form conducting tubular structures during differentiation. The effect of electrical stimulation on the differentiation of C2C12 myoblasts is also monitored by the impedance sensor at 0.82 kHz (Figure 5i). Under high stimulation, faster and greater impedance decreases are observed than other conditions owing to enhanced differentiation and subsequent myotube formation.

2.5. Electrical Stimulation and Recording for Electrophysiology In Vivo

Contraction and release of normal skeletal muscle tissues are controlled by depolarization and repolarization of the muscle electrical potential, i.e., EMG changes, which are elicited by

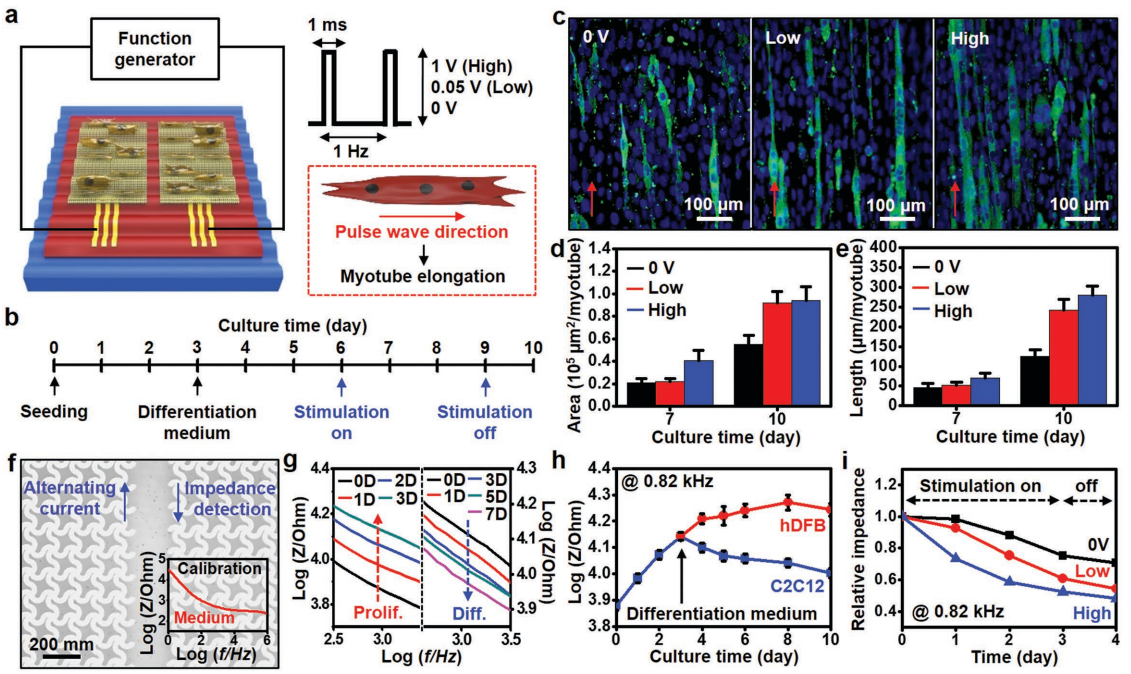

Figure 5. Electrical stimulation and physiological monitoring of C2C12 myoblasts using a buckled mesh-patterned graphene electrode in vitro. a) Schematic illustration of buckled mesh-patterned graphene electrode-mediated electrical stimulation to accelerate the differentiation of C2C12 myoblasts. Monophasic square wave pulses are applied with three different voltages, including 1 V (High), 0.05 V (Low), and 0 V. The red box at the lower right shows that the pulse wave is stimulated in the direction of myotube elongation. b) Timetable of cell culture. c) Fluorescence microscopy images of aligned and elongated C2C12 myotubes upon application of three different pulses. The red arrows indicate the direction of the pulse waves. d,e) Plots of d) myotube areas and e) lengths at day 7 (1 d after stimulation begins) and day 10 (1 d after stimulation is removed) differentiation time points. f) Optical microscopic image of graphene meshes (background image) and their impedance sensing mechanism. The bottom right inset shows the impedance curve under growth medium measured from 1 Hz to 1 MHz with a bias voltage of 0.01 V. g) Impedance curve of C2C12 myoblasts according to the proliferation (Prolif.) and the differentiation (Diff.) procedures. h) The impedance curve of C2C12 myoblasts measured at 0.82 kHz during culture, in comparison with that of human dermal fibroblasts (hDFB). i) The impedance values measured at 0.82 kHz as the electrical stimulation is applied. Black, red, and blue curves indicate three different pulse waves: 0 V, Low (0.05 V), and High (1 V), respectively. d,e,h) Quantitative data are acquired in quadruple ($n = 4$).

action potential signals from the central nervous system. Body movements in daily life are accompanied by muscle contraction/release and changes of EMG. The accurate and continuous recording of EMG through stable and reliable biointerfaces, therefore, is of high importance in electrodiagnosis of many motion-related neuromuscular diseases. Furthermore, electrical muscle stimulation is a promising procedure to enhance and recover the strength and function of diseased/wounded skeletal muscles.[54] For the electrical muscle stimulation therapy, programed impulses mimicking normal action potential patterns are highly effective.[54] The soft biointerface formed by the cell-sheet–graphene hybrid system is an appropriate tool for this diagnosis and therapy procedure.

To investigate electrophysiological applicability of the cell-sheet–graphene hybrid device in vivo, we implanted it onto the hind limb skeletal muscle region of a nude mouse and evaluated effectiveness of its electrical stimulation and EMG sensing function. The electrical stability of the cell-sheet–graphene hybrid under electrically active states (recording and stimulation) is well maintained without degradations of the electrode and the cell sheet as shown in Figure S9 in the Supporting Information. Soft nature of the cell-sheet–graphene hybrid forms a high quality biointerface. The effective electrical stimulation[55] (with 0.5 V; 1.25 mA and 1 V; 2.5 mA) on hind limb skeletal muscles is confirmed by subsequent twitching motions of the murine leg (**Figure 6**a, top; schematic illustration of experimental setups is shown in Figure S10 in the Supporting Information). Simultaneous electrical recording via the cell-sheet–graphene hybrid electrodes is shown in Figure 6a, bottom. Also, we evaluated the stimulating (Figure 6b) and recording (Figure S11c, Supporting Information) efficiencies of the device to the direction of muscle depth in ex vivo models. The low contact impedance of cell-sheet–graphene hybrid (Figure S11d, Supporting Information) enhances signal transduction efficiencies of electrical stimulation and recording in vivo. These high efficiencies are achieved with formation of the conducting myotube in the myoblast cell sheet (Figure S12, Supporting Information). Both stimulation to and recording from deep muscles using cell-sheet–graphene hybrid electrodes are effective. Figure 6c shows the EMG recording during hind limb skeletal muscle movements from an anesthetized (red) and unanesthetized (blue; after awakening from anesthesia) nude mouse. The top and bottom blue data show the raw and processed EMG signals from an unanesthetized mouse. No signal is detected in the anesthetized condition (red; bottom), which confirms the quality of the EMG data to discriminate against noise. Meanwhile, consideration of extrinsic (e.g., power line noise and cable motion artifact) and intrinsic

DOI: 10.1002/adfm.201504578

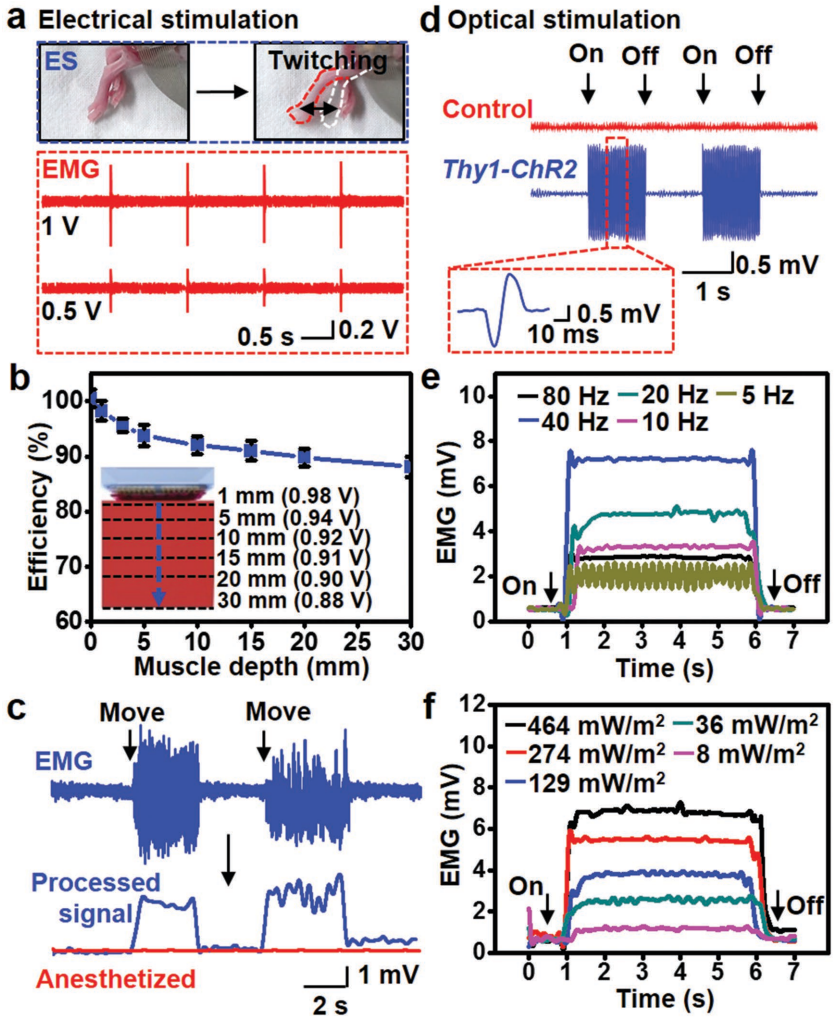

Figure 6. Electrophysiological and optogenetic investigations of implantable cell-sheet–graphene hybrids. a) Images of twitches elicited by electrical stimulation (1 V, 2.5 mA, 1 Hz) from the cell-sheet–graphene hybrid (top blue box) and the raw EMG signals (bottom red box) from two different electrical signals (1 V, 3.8 mA, 1 Hz; 0.5 V, 1.9 mA, 1 Hz) applied by a Pt electrode. b) Stimulating efficiency toward the direction of muscle depth in ex vivo models. The efficiency of electrical stimulation is decreased to ≈90% as the muscle depth is increased. For evaluating the stimulation efficiency, 1 V electrical signal is applied using the cell-sheet–graphene hybrid, and its signal is read at each depth from the Au electrode. c) Measurement of the EMG signals by the cell-sheet–graphene hybrid during muscle contractions of the murine leg. The top blue curve shows the raw EMG signal and the bottom blue curve shows the processed EMG signal (root-mean-square value). The bottom red curve shows the processed EMG signal of an anesthetized mouse. d) Raw EMG signals during LED on/off states. The blue and red curves represent the EMG signals from the transgenic and wild type mice, respectively. The red box shows a single unit of EMG signal. The frequency and intensity of the LEDs are fixed at 40 Hz and 464 mW m^{-2} (intensity after penetration of the hybrid). e,f) Plots of processed EMG recordings (root-mean-square value) at e) various frequencies, and f) light intensities of optical stimulation.

(e.g., thermal noise and electrode-tissue interface noise) noises during the EMG measurement is important.[56] Improvement of the electrochemical properties (low impedance and high capacitance) of the electrode can reduce the electrode–tissue interface noises.[18,53,56] Under same condition of the EMG measurement, therefore, the cell-sheet–graphene hybrid electrode shows the improved signal-to-noise ratio (Figure S13, Supporting Information), particularly in high amplification conditions (Figure S7, Supporting Information). The same cell-sheet–graphene hybrid system can be applied for EMG measurements on skin. Because of the conformal integration of the soft cell-sheet–graphene hybrid device with the human epidermis, human EMG signals are successfully measured (Figure S14, Supporting Information).[57]

2.6. Optical Stimulation and Electrophysiological Recording In Vivo

Optogenetics is an emerging stimulation technique that uses light instead of electrical impulses to excite genetically modified neurons that express light-sensitive proteins such as channelrhodopsin.[17,21,22,58] The optical stimulation of secondary motor cortex and/or peripheral motor neurons, which targets skeletal muscle improvement, provides enhanced therapeutic effects with low fatigue as compared to existing electrical stimulation methods.[21,58] Recording electrophysiological signals from optically stimulated target tissues is another important requirement. Conventional opaque metal electrodes, however, do not allow light to pass through them. Therefore, the intrinsic spatial mismatch between the stimulated tissue positioned immediately below the light source and the electrode position, typically located near the light source, devalues optogenetic approaches. Transparent and conforming electrodes including graphene electrodes have been recently highlighted as providing the spatial overlap of stimulation and recording positions.[18,59] The transparent cell-sheet–graphene hybrid described herein allows high quality biointerfacing for real time recordings as well as spatially synchronized optical stimulations.

To investigate the capabilities of the cell-sheet–graphene hybrid in optical stimulation and simultaneous recording, it is implanted onto the hind limb muscle region of a ChR2-expressing transgenic mouse (*Thy1-ChR2*)[21] and a blue LED of 470 nm wavelength is placed on top (the detailed experimental setup is shown in Figure S15 in the Supporting Information). The LED is controlled by a function generator to apply optical impulses whose frequency and intensity varied between 5 and 80 Hz and between 8 and 464 mW m^{-2}, respectively. The light intensity before and after passing through the device is shown in Figure S16 in the Supporting Information, which is high enough to stimulate deep muscles.[60] Optical stimulation-induced muscle activation and EMG signals are recorded simultaneously (40 Hz, 464 mW m^{-2} fixed; Figure 6d).

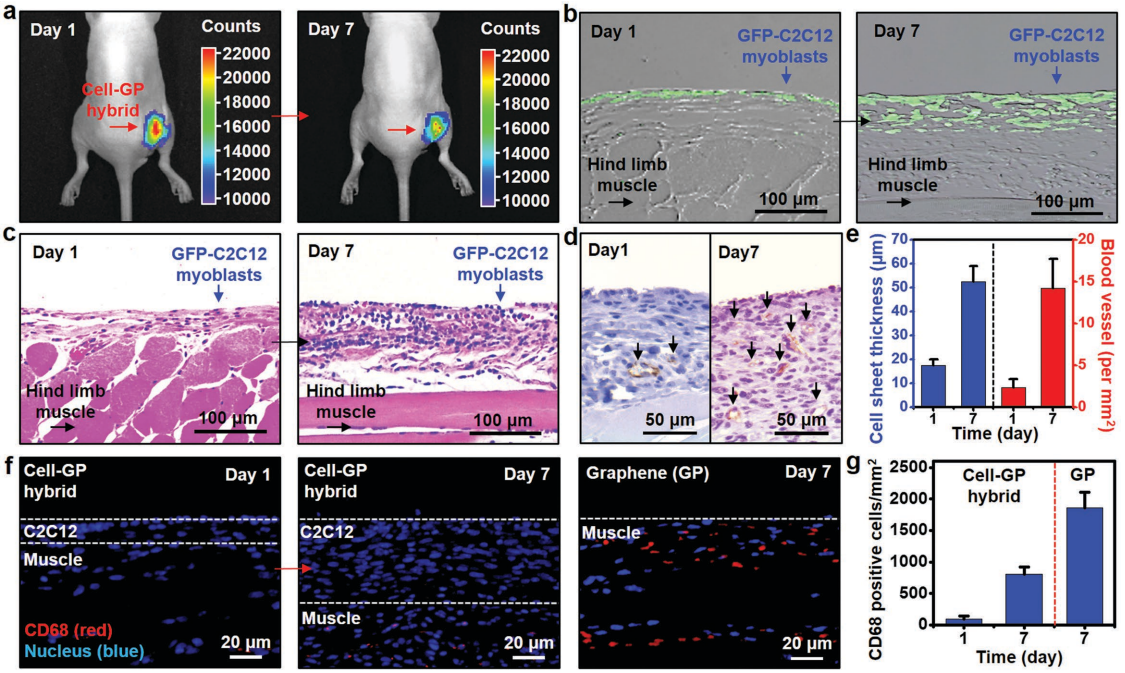

Figure 7. Investigation of the therapeutic effect of cell-sheet–graphene hybrids during implantation in mouse hind limb skeletal muscle. a) In vivo fluorescence images at 1 d (left) and 7 d (right) after the implantation of cell-sheet–graphene hybrids labeled with cell tracers (DiD). b) The proliferation of implanted GFP-C2C12 myoblasts at 1 d (left) and 7 d (right) after implantation. c) Hematoxylin and eosin staining of the operated hind limb at 1 d (left) and 7 d (right) after implantations for morphological observation. d) Formation of new vessels (black arrows) in the region of implantation at 1 d (left) and 7 d (right) after implantation. e) Plots of cell sheet thickness and the number of angiogenic vessels in the operated hind limb during 1 and 7 d after implantation. f,g) Fluorescence f) images and g) plots for observing the formation of high quality biointerface by immunostaining of operated hind limb muscle using anti-CD68 antibody (red fluorescence; macrophages) and counterstained with DAPI (blue fluorescence; nuclei). e,g) Quantitative data are acquired in quadruple ($n = 4$).

Twitching motions of the transgenic mouse leg are observed during optical stimulations. Optimized conditions of the light impulses for maximum excitation of peripheral motor neurons are experimentally determined through recording EMG signals under different light frequencies and intensities.[21,60] Figure 6e shows the processed EMG signals to present their amplitudes[61] under different frequencies (464 mW m^{-2} is fixed) of light impulses applied to hind limb muscles (filtered EMG shown in Figure S17 in the Supporting Information). We found that 40 Hz optical stimulation shows the highest amplitude of EMG. The plateau potential increases as the frequency of optical stimulation increases (Figure S17, Supporting Information).[60] The amplitude of EMG signal at the frequency of 80 Hz, however, is decreased because the depolarization continues from the delay of repolarization.[60] Figure 6f shows the processed EMG signals of different light intensities (40 Hz is fixed) ranging from 8 to 464 mW m^{-2} (filtered EMG shown in Figure S18 in the Supporting Information). The light intensity of 464 mW m^{-2} shows the highest amplitude of EMG; the amplitude of EMG decreases as the light intensity decreases.[21,60]

2.7. In Vivo Therapeutic Application of the Cell Sheet

The cell sheet in the cell-sheet–graphene hybrid not only enhances the conformal biointerface but also provides inherent therapeutic effects. The activities of the implanted cell sheet integrated in the cell-sheet–graphene hybrid are observed by transfecting the C2C12 myoblasts with green fluorescent protein (GFP; GFP-C2C12 myoblasts). We implanted the cell-sheet–graphene hybrid incorporating confluent and well-differentiated GFP-C2C12 myoblasts onto the hind limb skeletal muscles of nude mice. **Figure 7**a shows that the cell-sheet–graphene hybrid is capable of maintaining its organization at the operation site for 1 and 7 d after the implantation. Fluorescence is detected at the implanted site during the 7 d period, whereas no signal is observed from the opposite hind limb site (control). The cell-sheet–graphene hybrid is observed in vivo using the IVIS Lumina imaging system (Perkin Elmer, Waltham, MA, USA) via GFP-C2C12 myoblasts labeled with a cell tracer (DiD) to avoid the codetection of native tissue autofluorescence. Spatial confinement of the implanted cells in the cell-sheet–graphene hybrid for more than 7 d with well-maintained organization can elicit maximized therapeutic functions at wound sites.[35]

The growth of the GFP-C2C12 myoblasts at the implanted site is shown in Figure 7b. Fluorescence microscope images are obtained from sectioned tissue slices. While a single layer of GFP-C2C12 myoblasts is detected 1 d after implantation, several layers on the native muscle are observed 7 d after implantation, which confirms the efficient proliferation of transplanted myoblasts from the cell-sheet–graphene hybrid. Images of hematoxylin and eosin staining are consistent with

DOI: 10.1002/adfm.201504578

the fluorescence images (Figure 7c). These results further confirm that implanted GFP-C2C12 myoblasts survive and proliferate in vivo. New vessel formation, i.e., angiogenesis, is essential in this regeneration particularly for nutrition supply and gas exchange. Figure 7d shows the enhancement of local angiogenesis 7 d after implantation. CD31 staining of angiogenic vessels indicates the growth of the GFP-C2C12 myoblasts in/near the implanted sites. The quantified data of the thickness of cell growth and the number of angiogenic vessels from the microscope images are plotted in Figure 7e, which corroborates the therapeutic effect of the cell-sheet–graphene hybrid. The localization of highly differentiated C2C12 myoblasts in the implanted cell-sheet–graphene hybrid enhances vascularization, regeneration of skeletal muscles, and functional recovery.[31,62] Furthermore, the fluorescence images indicate that C2C12 myoblasts on the surface of graphene electrodes suppress the recruitment of CD68-positive macrophages at the implanted site (Figure 7f). Without the cell sheet, the device can cause acute immune responses. Its quantitative data is plotted in Figure 7g. These results support that the cell-sheet–graphene hybrid is highly effective for both the diagnosis and treatment of skeletal muscle tissue damages.

3. Conclusion

The stretchable and transparent biointerface using a cell-sheet–graphene hybrid offers a new strategy for multifunctional implantable devices. It features high quality electrophysiological sensing, electrical and/or optical stimulation treatment, and regeneration therapy by hybridized cells. The integrated system is biocompatible and highly effective as a soft implantable device for skeletal muscle tissue. The buckled graphene mesh aligns the cultured cells and enhances their proliferation and differentiation as well as provides mechanical stretchability to the system. Furthermore, it acts as an electrical stimulator and an impedance sensor for the controlled culture of C2C12 myoblasts and their continuous monitoring in vitro. The well fabricated, transparent, and stretchable cell-sheet–graphene hybrid is implanted on the hind limb muscle of mouse for electromyographic monitoring and the treatment of normal and transgenic muscles with electrical and optical stimulation in vivo. The cell sheet on the hybrid provides therapeutic function onto implanted tissues as well as forming a high quality biointerface without any host immune responses. These advances open a new pathway to the next-generation multifunctional soft bioelectronics.

4. Experimental Section

Cellular Characteristics on the Buckled Graphene Mesh: To observe the alignment of cytoskeletal actin filaments, the C2C12 myoblasts were counter-stained with rhodamine phalloidine (Life Technologies) and 4′,6-diamidino-2-phenylindole (DAPI). Cells were also immunostained with antimyosin heavy chain antibodies (1:100 dilution; Abcam) and Alexa Fluor 488 donkey antimouse IgG (1:100 dilution; Abcam) to observe myotube formation. The stained samples were observed and captured by a fluorescence microscope (Eclipse Ti, Nikon). The images were analyzed by Image-Pro Plus software (Media Cybernetics).

Electrochemical Characteristics of Buckled Graphene Mesh: Impedance, conductance, and CV were measured by electrochemical workstation (CHI660E, CH Instruments). Measurements of impedance and conductance were conducted with three-electrode configuration (buckled graphene mesh, Ag/AgCl, and Pt electrode), and CV was conducted with two-electrode configuration (buckled graphene mesh and Ag/AgCl electrode) in pH 7.0 PBS solution.

Electrical Characteristics of C2C12 Myoblasts on the Cell-Sheet-Graphene Hybrid: For electrical stimulation, monophasic square wave pulses were applied to culturing C2C12 myoblasts via the hybrid. The parameters of the pulses, including frequency, duration, and amplitude were controlled by a function generator (33500B, Agilent Technologies). During electrical stimulation, the cells were cultured in an incubator under standard culture conditions. For monitoring the impedance changes, the electrodes of the hybrid were connected and measured using an electrochemical workstation (CHI660E, CH Instruments).

In Vivo Mouse Model: The experiments on the animals used for the optogenetics study were approved by the Animal Care Committees at the Korea Institute of Science and Technology. Lab-bred 9–12 week-old *Thy1-ChR2* or C57BL/6 control mice were anesthetized with 2% avertin (tribro-moethyl alcohol/tertiary amyl alcohol), and the hind limb was surgically incised for the implantation. The experiments on animals for in vivo implantation and cell therapy were approved by the Animal Care Committees at Seoul National University Hospital. Six-week-old male BALB/c nude mice were anesthetized by intraperitoneal injection with a mixture of zolazepam and xylazine. The skin was surgically incised to 1.5 cm in the ventral aspect of the right thigh.

Electrical and Optical Characteristics of the Cell-Sheet-Graphene Hybrid In Vivo: For electrical stimulation, monophasic square wave pulses were applied to the skeletal muscle and controlled by a function generator. For optical stimulation, the frequency and intensity of a 470 nm LED lamp (1.5 W T10 blue LED, Sungetace) on the top of the device was controlled by a function generator. The EMG signal of the skeletal muscle was measured using a data acquisition equipment (DAQ; National Instruments) with the LabVIEW software (encoded with 60 Hz notch filter). A voltage amplifier (Stanford Research Systems) was additionally used for filtering (10 Hz of high-pass filter and 300 Hz of low-pass filter) and amplifying (×500 of gain) the signals. The EMG signal was processed using MATLAB software (MathWorks). To obtain the root-mean-square signal, the data are treated with filtering (cut off the data at 100 Hz), rectifying (cut off the negative part), smoothing, and root-mean-square processing, sequentially.

Histology: For sample preparation, all tissues were fixed in paraffin and sectioned to 4 mm thickness. The prepared sections were dewaxed, hydrated, and treated with 0.01% protease XXIV in PBS. To visualize GFP-expressing myoblasts, the specimens were stained with primary anti-GFP antibodies (Santa Cruz Biotechnology) according to the manufacturer's instructions. Alexa Fluor 488-conjugated secondary antibodies (Invitrogen) were used to visualize protein expression. Images were obtained by an inverted fluorescence microscope. Histology samples for morphology visualization were stained by hematoxylin and eosin using standard protocols, and vascularization detection was performed using immunohistochemistry with anti-CD31 antibodies (Novus Biologicals) followed by staining with a 3,3′-diaminobenzidine (Dako) peroxidase substrate. Macrophages were also immunohistochemically stained with anti-CD68 antibodies (Novus Biologicals) and Alexa Fluor 647-conjugated secondary antibodies (Invitrogen). The histologic samples were observed using an optical and fluorescence microscope.

Supporting Information

Supporting Information is available from the Wiley Online Library or from the author.

Acknowledgements

S.J.K. and K.W.C. contributed equally to this work. This work was supported by IBS-R006-D1. N. L. acknowledges the US NSF CMMI award under Grant No. 1301335.

Received: October 26, 2015
Revised: February 3, 2016
Published online:

[1] D. Khodagholy, T. Doublet, P. Quilichini, M. Gurfinkel, P. Leleux, A. Ghestem, E. Ismailova, T. Hervé, S. Sanaur, C. Bernard, G. G. Malliaras, *Nat. Commun.* **2013**, *4*, 1575.
[2] B. Emeryk-Szajewska, J. Kopeć, *Electromyogr. Clin. Neurophysiol.* **2008**, *48*, 265.
[3] I. Hausmanowa-Petrusewicz, A. Karwańska, *Muscle Nerve* **1986**, *9*, 37.
[4] S. Rissanen, M. Kankaanpää, M. P. Tarvainen, J. Nuutinen, I. M. Tarkka, O. Airaksinen, P. A. Karjalainen, *Physiol. Meas.* **2007**, *28*, 1507.
[5] I. R. Minev, P. Musienko, A. Hirsch, Q. Barraud, N. Wenger, E. M. Moraud, J. Gandar, M. Capogrosso, T. Milekovic, L. Asboth, R. F. Torres, N. Vachicouras, Q. Liu, N. Pavlova, S. Duis, A. Larmagnac, J. Vörös, S. Micera, Z. Suo, G. Courtine, S. P. Lacour, *Science* **2015**, *347*, 159.
[6] S. Lim, D. Son, J. Kim, Y. B. Lee, J. Song, S. Choi, D. J. Lee, J. H. Kim, M. Lee, T. Hyeon, D.-H. Kim, *Adv. Funct. Mater.* **2015**, *25*, 375.
[7] D. Son, J. Lee, S. Qiao, R. Ghaffari, J. Kim, J. E. Lee, C. Song, S. J. Kim, D. J. Lee, S. W. Jun, S. Yang, M. Park, J. Shin, K. Do, M. Lee, K. Kang, C. S. Hwang, N. Lu, T. Hyeon, D.-H. Kim, *Nat. Nanotechnol.* **2014**, *9*, 397.
[8] M. K. Choi, O. K. Park, C. Choi, S. Qiao, R. Ghaffari, J. Kim, D. J. Lee, M. Kim, W. Hyun, S. J. Kim, H. J. Hwang, S.-H. Kwon, T. Hyeon, N. Lu, D.-H. Kim, *Adv. Healthc. Mater.* **2016**, *5*, 80.
[9] M. K. Choi, I. Park, D. C. Kim, E. Joh, O. K. Park, J. Kim, M. Kim, C. Choi, J. Yang, K. W. Cho, J.-H. Hwang, J.-M. Nam, T. Hyeon, J. H. Kim, D.-H. Kim, *Adv. Funct. Mater.* **2015**, *25*, 7109.
[10] R. Normann, D. McDonnall, G. Clark, *Conf. Proc. IEEE. Eng. Med. Biol. Soc.* **2005**, *7*, 7644.
[11] L. Xu, S. R. Gutbrod, A. P. Bonifas, Y. Su, M. S. Sulkin, N. Lu, H. J. Chung, K. I. Jang, Z. Liu, M. Ying, C. Lu, R. C. Webb, J.-S. Kim, J. I. Laughner, H. Cheng, Y. Liu, A. Ameen, J.-W. Jeong, G.-T. Kim, Y. Huang, I. R. Efimov, J. A. Rogers, *Nat. Commun.* **2014**, *5*, 3329.
[12] D.-H. Kim, N. Lu, R. Ma, Y.-S. Kim, R.-H. Kim, S. Wang, J. Wu, S. M. Won, H. Tao, A. Islam, K. J. Yu, T.-I. Kim, R. Chowdhury, M. Ying, L. Xu, M. Li, H.-J. Chung, H. Keum, M. McCormick, P. Liu, Y.-W. Zhang, F. G. Omenetto, Y. Huang, T. Coleman, J. A. Rogers, *Science* **2011**, *333*, 838.
[13] J. Kim, M. Lee, H. J. Shim, R. Ghaffari, H. R. Cho, D. Son, Y. H. Jung, M. Soh, C. Choi, S. Jung, K. Chu, D. Jeon, S.-T. Lee, J. H. Kim, S. H. Choi, T. Hyeon, D.-H. Kim, *Nat. Commun.* **2014**, *5*, 5747.
[14] T. Sekitani, U. Zschieschang, H. Klauk, T. Someya, *Nat. Mater.* **2010**, *9*, 1015.
[15] K. Kuribara, H. Wang, N. Uchiyama, K. Fukuda, T. Yokota, U. Zschieschang, C. Jaye, D. Fischer, H. Klauk, T. Yamamoto, K. Takimiya, M. Ikeda, H. Kuwabara, T. Sekitani, Y.-L. Loo, T. Someya, *Nat. Commun.* **2012**, *3*, 723.
[16] S. Choi, J. Park, W. Hyun, J. Kim, J. Kim, Y. B. Lee, C. Song, H. J. Hwang, J. H. Kim, T. Hyeon, D.-H. Kim, *ACS Nano* **2015**, *9*, 6626.
[17] D.-W. Park, A. A. Schendel, S. Mikael, S. K. Brodnick, T. J. Richner, J. P. Ness, M. R. Hayat, F. Atry, S. T. Frye, R. Pashaie, S. Thongpang, Z. Ma, J. C. Williams, *Nat. Commun.* **2014**, *5*, 5258.
[18] D. Kuzum, H. Takano, E. Shim, J. C. Reed, H. Juul, A. G. Richardson, J. de Vries, H. Bink, M. A. Dichter, T. H. Lucas, D. A. Coulter, E. Cubukcu, B. Litt, *Nat. Commun.* **2014**, *5*, 5259.
[19] D. Khodagholy, J. N. Gelinas, T. Thesen, W. Doyle, O. Devinsky, G. G. Malliaras, G. Buzsáki, *Nat. Neurosci.* **2015**, *18*, 310.
[20] A. Williamson, M. Ferro, P. Leleux, E. Ismailova, A. Kaszas, T. Doublet, P. Quilichini, J. Rivnay, B. Rózsa, G. Katona, C. Bernard, G. G. Malliaras, *Adv. Mater.* **2015**, *27*, 4405.
[21] M. E. Llewellyn, K. R. Thompson, K. Deisseroth, S. L. Delp, *Nat. Med.* **2010**, *16*, 1161.
[22] T.-I. Kim, J. G. McCall, Y. H. Jung, X. Huang, E. R. Siuda, Y. Li, J. Song, Y. M. Song, H. A. Pao, R.-H. Kim, C. Lu, S. D. Lee, I.-S. Song, G. Shin, R. Al-Hasani, S. Kim, M. P. Tan, Y. Huang, F. G. Omenetto, J. A. Rogers, M. R. Bruchas, *Science* **2013**, *340*, 211.
[23] B. C.-K. Tee, A. Chortos, A. Berndt, A. K. Nguyen, A. Tom, A. McGuire, Z. C. Lin, K. Tien, W.-G. Bae, H. Wang, P. Mei, H.-H. Chou, B. Cui, K. Deisseroth, T. N. Ng, Z. Bao, *Science* **2015**, *350*, 313.
[24] D. A. LaVan, T. McGuire, R. Langer, *Nat. Biotechnol.* **2003**, *21*, 1184.
[25] D. Son, J. Lee, D. J. Lee, R. Ghaffari, S. Yun, S. J. Kim, J. E. Lee, H. R. Cho, S. Yoon, S. Yang, S. Lee, S. Qiao, D. Ling, S. Shin, J.-K. Song, J. Kim, T. Kim, H. Lee, J. Kim, M. Soh, N. Lee, C. S. Hwang, S. Nam, N. Lu, T. Hyeon, S. H. Choi, D.-H. Kim, *ACS Nano* **2015**, *9*, 5937.
[26] P. Couvreur, *Nat. Nanotechnol.* **2014**, *9*, 874.
[27] Y. Brudno, E. A. Silva, C. J. Kearney, S. A. Lewin, A. Miller, K. D. Martinick, M. Aizenberg, D. J. Mooney, *Proc. Natl. Acad. Sci. USA* **2014**, *111*, 12722.
[28] B. D. Cosgrove, P. M. Gilbert, E. Porpiglia, F. Mourkioti, S. P. Lee, S. Y. Corbel, M. E. Llewellyn, S. L. Delp, H. M. Blau, *Nat. Med.* **2014**, *20*, 255.
[29] J. J. Chong, X. Yang, C. W. Don, E. Minami, Y. W. Liu, J. J. Weyers, W. M. Mahoney, B. Van Biber, S. M. Cook, N. J. Palpant, J. A. Gantz, J. A. Fugate, V. Muskheli, G. M. Gough, K. W. Vogel, C. A. Astley, C. E. Hotchkiss, A. Baldessari, L. Pabon, H. Reinecke, E. A. Gill, V. Nelson, H.-P. Kiem, M. A. Laflamme, C. E. Murry, *Nature* **2014**, *510*, 273.
[30] M. B. Pabbruwe, E. Esfandiari, W. Kafienah, J. F. Tarlton, A. P. Hollander, *Biomaterials* **2009**, *30*, 4277.
[31] D. W. Kim, I. Jun, T.-J. Lee, J. h. Lee, Y. J. Lee, H.-K. Jang, S. Kang, K. D. Park, S.-W. Cho, B.-S. Kim, H. Shin, *Biomaterials* **2013**, *34*, 8258.
[32] J. F. Liao, Y. Qu, B. Y. Chu, X. N. Zhang, Z. Y. Qian, *Sci. Rep.* **2015**, *5*, 9879.
[33] J.-M. Seo, S. J. Kim, H. Chung, E. T. Kim, H. G. Yu, Y. S. Yu, *Mater. Sci. Eng. C* **2004**, *24*, 185.
[34] S. Defrère, M. Mestagdt, R. Riva, F. Krier, A. Van Langendonckt, P. Drion, C. Jérôme, B. Evrard, J.-P. Dehoux, J.-M. Foidart, J. Donnez, *Macromol. Biosci.* **2011**, *11*, 1336.
[35] S. J. Kim, H. R. Cho, K. W. Cho, S. Qiao, J. S. Rhim, M. Soh, T. Kim, M. K. Choi, C. Choi, I. Park, N. S. Hwang, T. Hyeon, S. H. Choi, N. Lu, D.-H. Kim, *ACS Nano* **2015**, *9*, 2677.
[36] P. O. Bagnaninchi, N. Drummond, *Proc. Natl. Acad. Sci. USA* **2011**, *108*, 6462.
[37] T.-H. Han, Y. Lee, M.-R. Choi, S.-H. Woo, S.-H. Bae, B. H. Hong, J.-H. Ahn, T.-W. Lee, *Nat. Photonics* **2012**, *6*, 105.
[38] S. P. Lacour, J. Jones, S. Wagner, T. Li, Z. Suo, *Proc. IEEE* **2005**, *93*, 1459.
[39] S. Bae, H. Kim, Y. Lee, X. Xu, J.-S. Park, Y. Zheng, J. Balakrishnan, T. Lei, H. R. Kim, Y. I. Song, Y.-J. Kim, K. S. Kim, B. Özyilmaz, J.-H. Ahn, B. H. Hong, S. Iijima, *Nat. Nanotechnol.* **2010**, *5*, 574.
[40] C. M. Stafford, C. Harrison, K. L. Beers, A. Karim, E. J. Amis, M. R. VanLandingham, H. C. Kim, W. Volksen, R. D. Miller, E. E. Simonyi, *Nat. Mater.* **2004**, *3*, 545.

[41] A. A. Sawyer, K. M. Hennessy, S. L. Bellis, *Biomaterials* **2005**, *26*, 1467.
[42] D.-H. Kim, N. Lu, R. Ghaffari, J. A. Rogers, *NPG Asia Mater.* **2012**, *4*, e15.
[43] N. Lu, D.-H. Kim, *Soft Robotics* **2013**, *1*, 53.
[44] D. Son, J. H. Koo, J. K. Song, J. Kim, M. Lee, H. J. Shim, M. Park, M. Lee, J. H. Kim, D.-H. Kim, *ACS Nano* **2015**, *9*, 5585.
[45] G. S. Jeong, D.-H. Baek, H. C. Jung, J. H. Song, J. H. Moon, S. W. Hong, I. Y. Kim, S.-H. Lee, *Nat. Commun.* **2012**, *3*, 977.
[46] C. Lee, X. Wei, J. W. Kysar, J. Hone, *Science* **2008**, *321*, 385.
[47] D. Huh, B. D. Matthews, A. Mammoto, M. Montoya-Zavala, H. Y. Hsin, D. E. Ingber, *Science* **2010**, *328*, 1662.
[48] D. Huh, D. C. Leslie, B. D. Matthews, J. P. Fraser, S. Jurek, G. A. Hamilton, K. S. Thorneloe, M. A. McAlexander, D. E. Ingber, *Sci. Transl. Med.* **2012**, *4*, 159ra147.
[49] D. E. Rassier, B. R. MacIntosh, W. Herzog, *J. Appl. Physiol.* **1999**, *86*, 1445.
[50] S. Jung, J. H. Kim, J. Kim, S. Choi, J. Lee, I. Park, T. Hyeon, D.-H. Kim, *Adv. Mater.* **2014**, *26*, 4825.
[51] E. T. McAdams, J. Jossinet, R. Subramanian, R. G. McCauley, *Conf. Proc. IEEE Eng. Med. Biol. Soc.* **2006**, *1*, 4594.
[52] M. Fernández, R. Pallás-Areny, *Biomed. Instrum. Technol.* **2000**, *34*, 125.
[53] Z. Yang, L. Hoang, Q. Zhao, E. Keefer, W. Liu, *Ann. Biomed. Eng.* **2011**, *39*, 1264.
[54] C. M. Gregory, C. S. Bickel, *J. Am. Phys. Ther. Assoc.* **2005**, *85*, 358.
[55] B. T. Zhang, S. S. Yeung, Y. Liu, H.-H. Wang, Y.-M. Wan, S.-K. Ling, H.-Y. Zhang, Y.-H. Li, E. W. Yeung, *BMC Cell Biol.* **2010**, *11*, 87.
[56] C. J. De Luca, L. D. Gilmore, M. Kuznetsov, S. H. Roy, *J. Biomech.* **2010**, *43*, 1573.
[57] W. H. Yeo, Y. S. Kim, J. Lee, A. Ameen, L. Shi, M. Li, S. Wang, R. Ma, S. H. Jin, Z. Kang, Y. Huang, J. A. Rogers, *Adv. Mater.* **2013**, *25*, 2773.
[58] S. Zhao, J. T. Ting, H. E. Atallah, L. Qiu, J. Tan, B. Gloss, G. J. Augustine, K. Deisseroth, M. Luo, A. M. Graybiel, G. Feng, *Nat. Methods* **2011**, *8*, 745.
[59] H. Lee, Y. Lee, C. Song, H. R. Cho, R. Ghaffari, T. K. Choi, K. H. Kim, Y. B. Lee, D. Ling, H. Lee, S. J. Yu, S. H. Choi, T. Hyeon, D.-H. Kim, *Nat. Commun.* **2015**, *6*, 10059.
[60] T. Bruegmann, T. Van Bremen, C. C. Vogt, T. Send, B. K. Fleischmann, P. Sasse, *Nat. Commun.* **2015**, *6*, 7153.
[61] D. M. Pinciveroa, R. C. Greenb, J. D. Markb, R. M. Campyc, *J. Electromyogr. Kinesiol.* **2000**, *10*, 189.
[62] S. Levenberg, J. Rouwkema, M. Macdonald, E. S. Garfein, D. S. Kohane, D. C. Darland, R. Marini, C. A. van Blitterswijk, R. C. Mulligan, P. A. D'Amore, R. Langer, *Nat. Biotechnol.* **2005**, *23*, 879.

ADVANCED FUNCTIONAL MATERIALS

Supporting Information

for *Adv. Funct. Mater.*, DOI: 10.1002/adfm.201504578

Stretchable and Transparent Biointerface Using Cell-Sheet–Graphene Hybrid for Electrophysiology and Therapy of Skeletal Muscle

Seok Joo Kim, Kyoung Won Cho, Hye Rim Cho, Liu Wang, Sung Young Park, Seung Eun Lee, Taeghwan Hyeon, Nanshu Lu, Seung Hong Choi, and Dae-Hyeong Kim**

Supporting Information

Stretchable and Transparent Bio-Interface Using Cell-Sheet-Graphene Hybrid for Electrophysiology and Therapy of Skeletal Muscle

Seok Joo Kim[†], Kyoung Won Cho[†], Hye Rim Cho, Liu Wang, Sung Young Park, Seung Eun Lee, Taeghwan Hyeon, Nanshu Lu, Seung Hong Choi, Dae-Hyeong Kim**

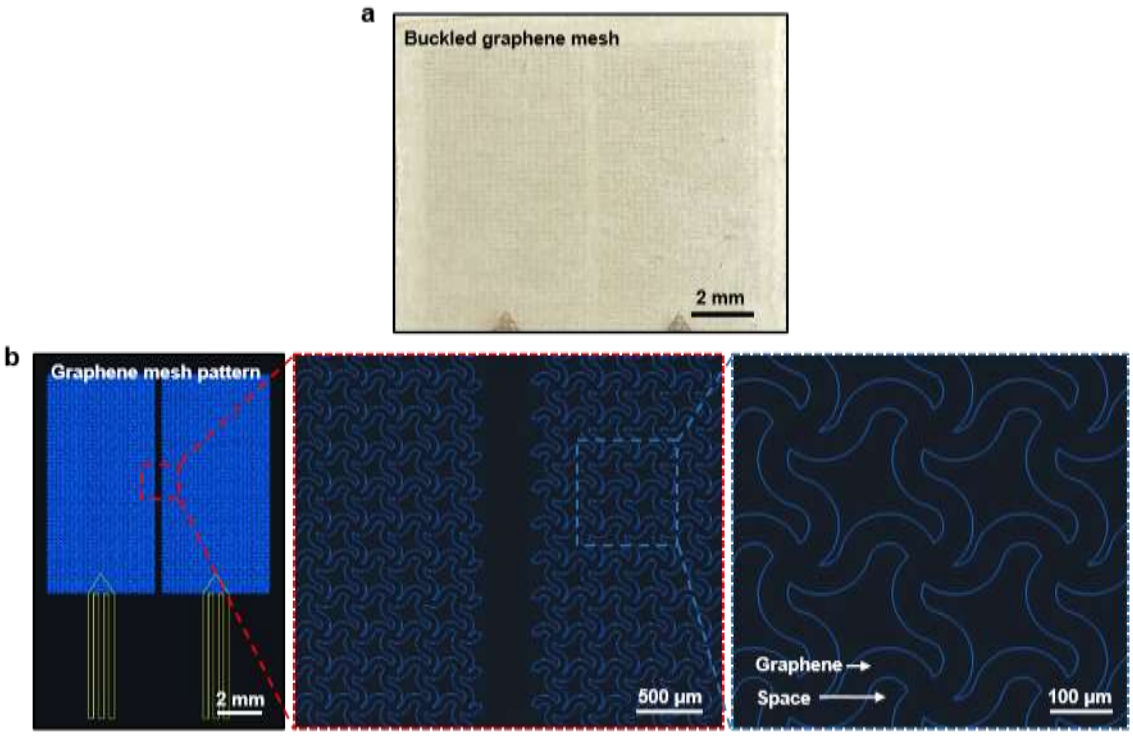

Figure S1. Photographic image (a) and AutoCAD designs (b) of mesh-patterned graphene electrodes. Serpentine electrodes (width of 50 μm) patterned into mesh structure. Two mesh electrodes are spaced 300 μm apart.

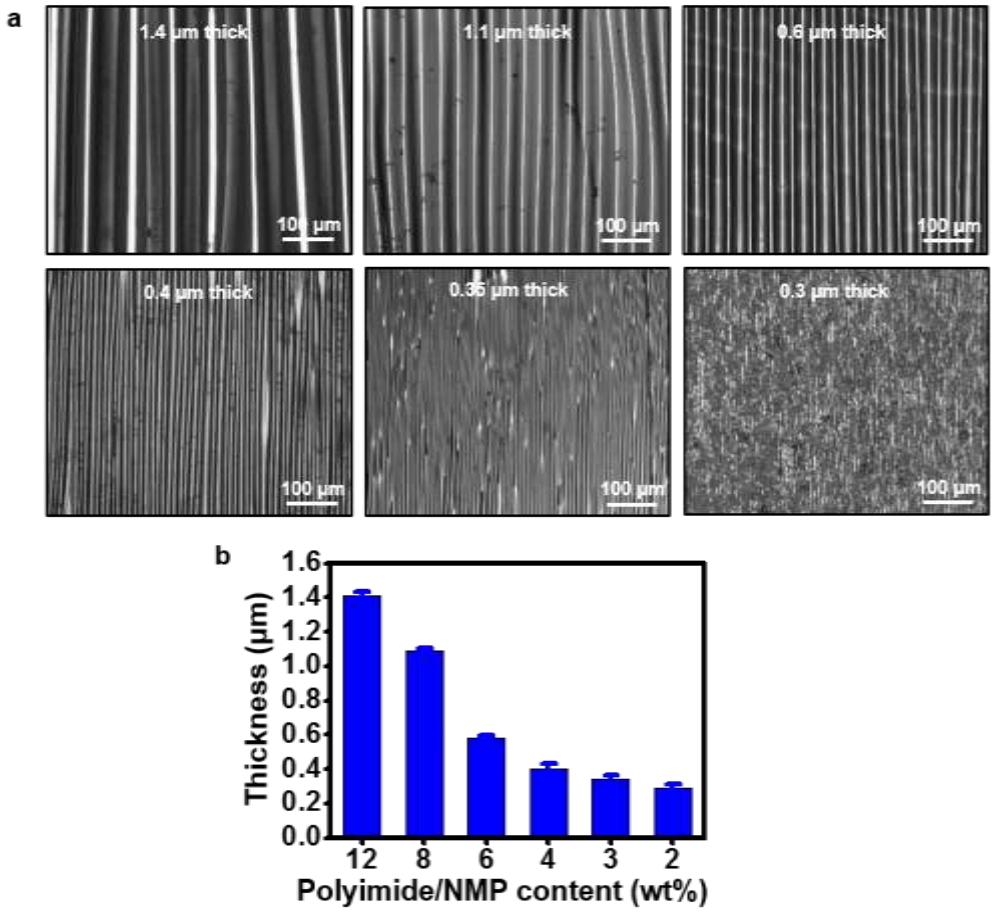

Figure S2. Characterization of the wavelengths of buckled structure. a) Optical microscopic images of uniform buckled structure of different wavelengths according to the PI/graphene layer thickness (from 1.4 μm to 0.3 μm), b) A plot of PI/graphene layer thickness versus polyimide/*N*-Methyl-2-pyrrolidone (NMP) concentration in weight percent.

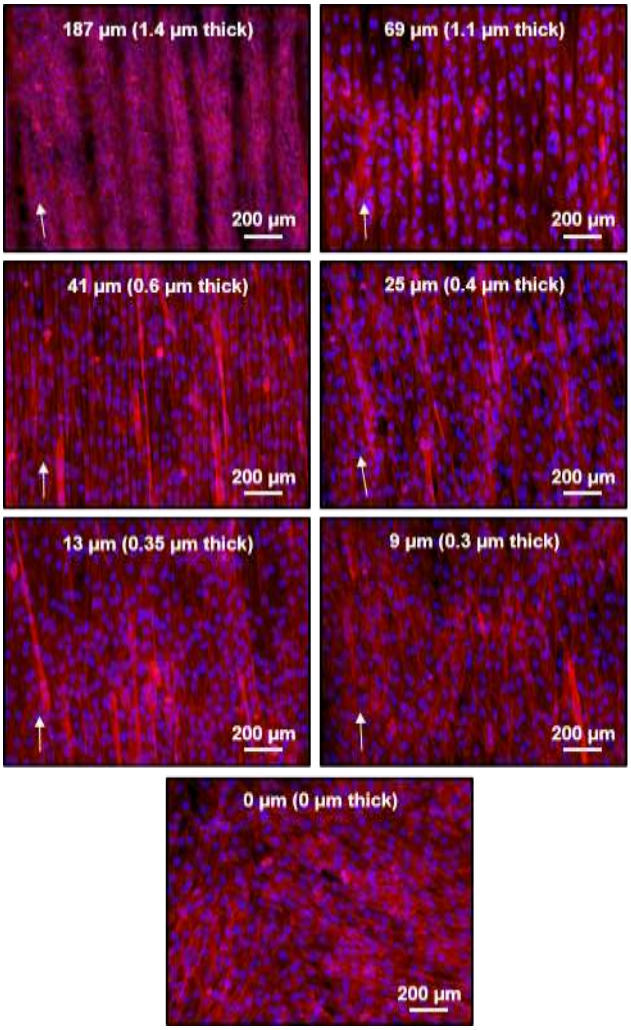

Figure S3. Fluorescence microscopic images of cell alignments in respect to the wavelengths of anisotropic buckled graphene mesh. C2C12 myoblasts are cultured on the 7 different wavelengths (from 0 μm (0 μm thick) to 187 μm (1.4 μm thick)) of uniform buckled structures to find the wavelength of buckled structure for best cell alignments. Each sample is observed after 3 days of culture by a fluorescence microscopy.

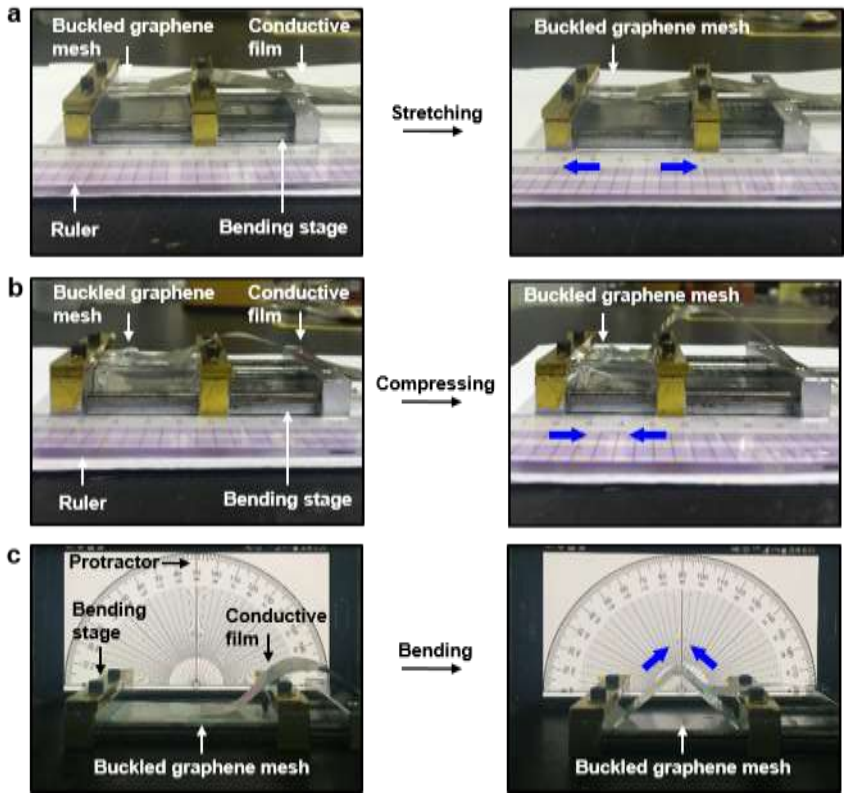

Figure S4. Images of experiment setups for stretching (a), compressing (b), and bending (c) tests. To conduct the mechanical deformation tests, resistances of the electrodes, including those of flat graphene sheet, buckled graphene sheet, and buckled graphene mesh, are measured, while deforming the sample using a custom-made manual bending stage to apply external strains.

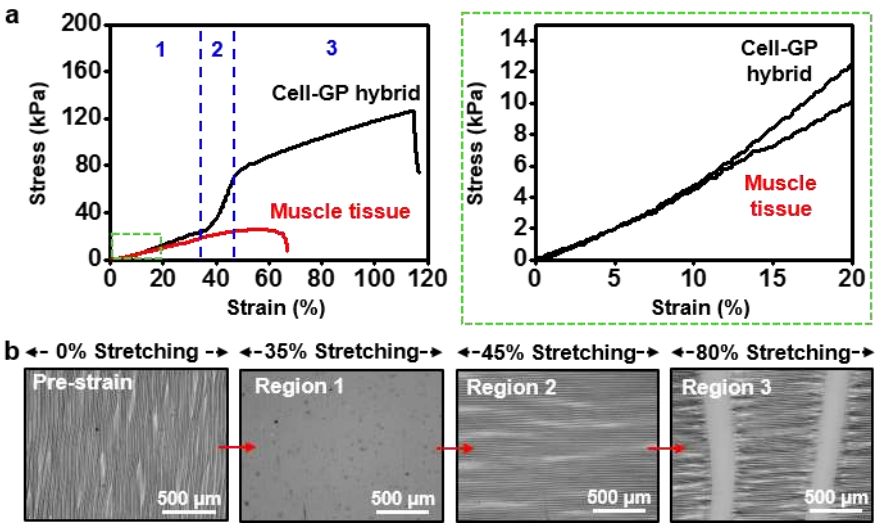

Figure S5. System modulus of cell-sheet-graphene hybrid. a) Plot of stress-strain curve of cell-sheet-graphene hybrid (Cell-GP hybrid; black) and muscle tissue (red). The hybrid contains 3 distinct regions in the system modulus curve: i) elastic stretching of the hybrid due to buckled topology (~35% of strain), ii) the endurance of polyimide membrane which supports cell sheet and mesh-patterned graphene electrodes (~45% of strain), and iii) the elastic stretching of PDMS after complete fracture of polyimide membrane (~115% of strain). The green-dotted box shows the plot of initial strain region (~20%). b) Microscopic images of Cell-GP hybrid at each regions in the system modulus curve.

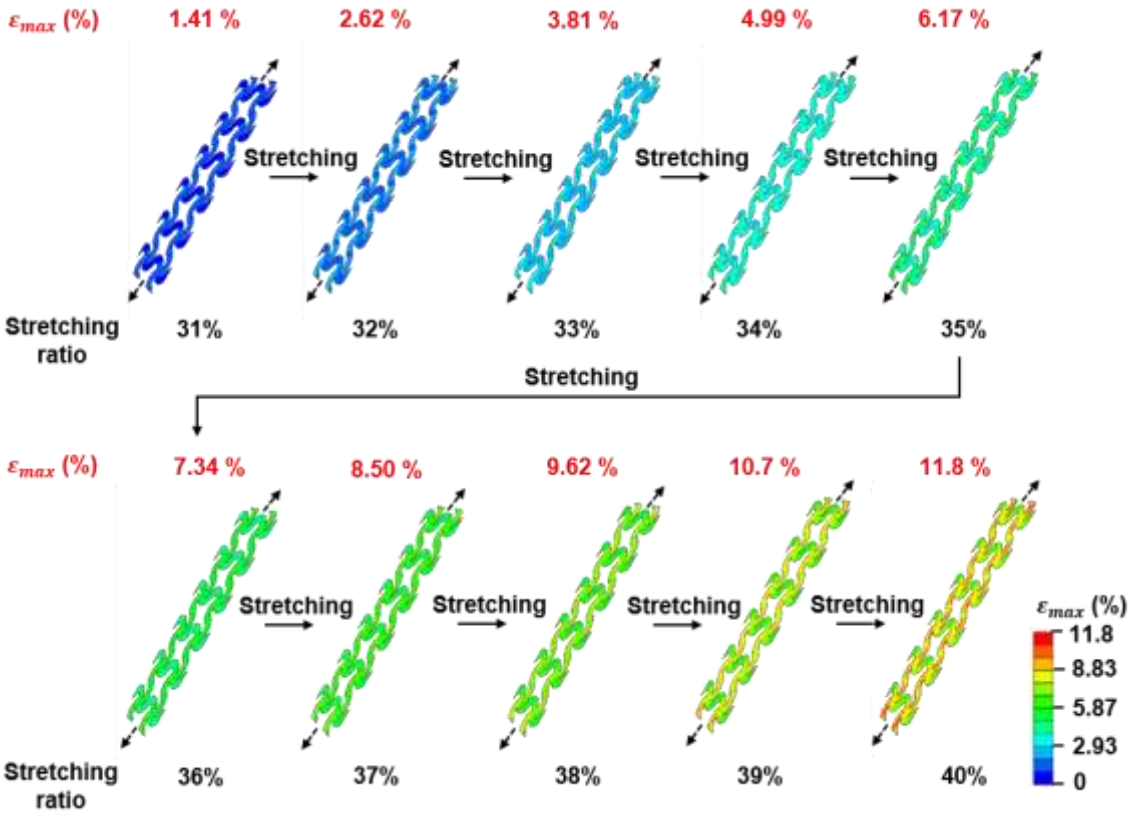

Figure S6. Maximum principal strain distribution computed by FEM simulation for the buckled graphene mesh after applying external strain.

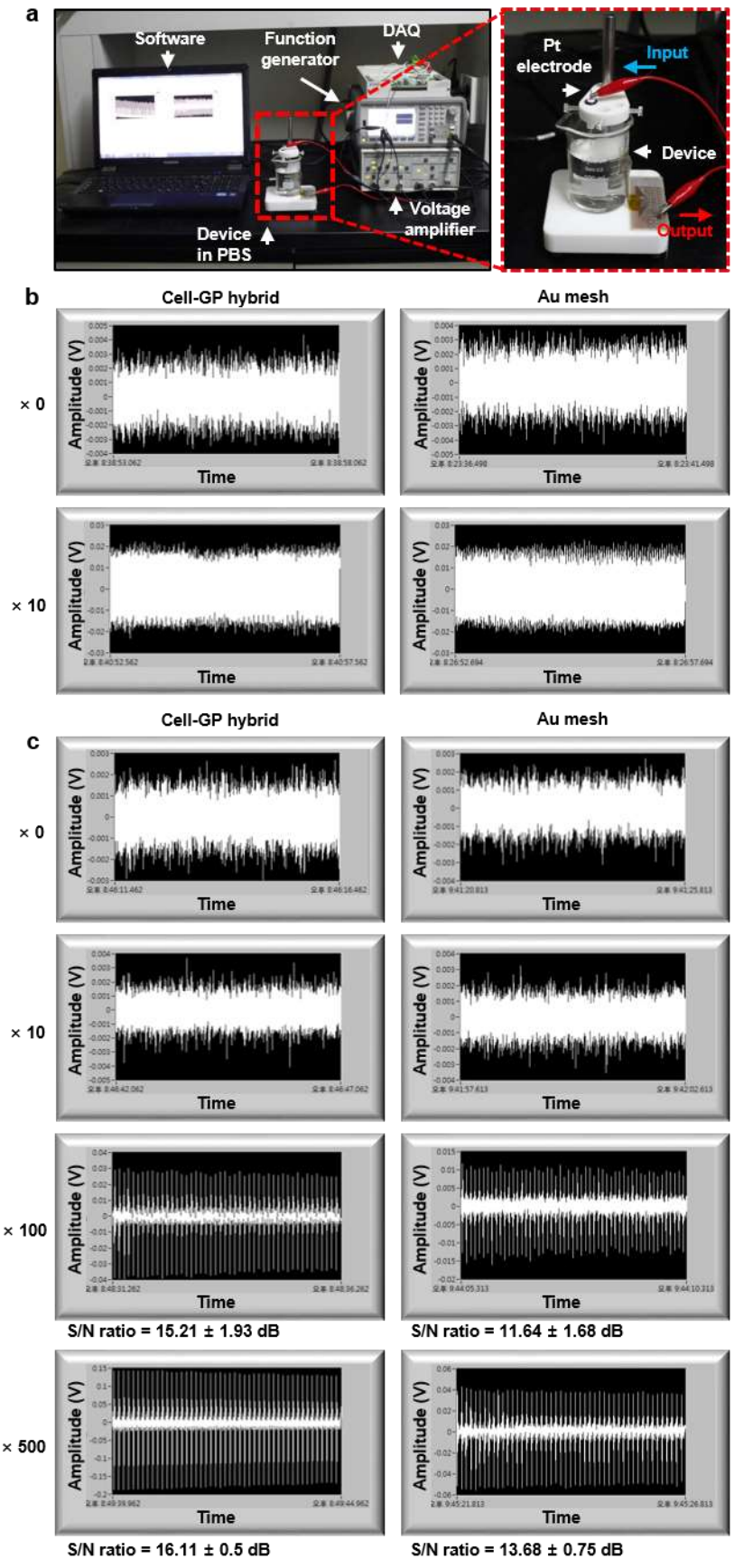
a
Software
Function generator
DAQ
Device in PBS
Voltage amplifier
Pt electrode
Input
Device
Output
b
Cell-GP hybrid
Au mesh
× 0
× 10
Amplitude (V)
Time
c
Cell-GP hybrid
Au mesh
× 0
× 10
× 100
× 500
Amplitude (V)
Time
S/N ratio = 15.21 ± 1.93 dB
S/N ratio = 11.64 ± 1.68 dB
S/N ratio = 16.11 ± 0.5 dB
S/N ratio = 13.68 ± 0.75 dB

Figure S7. Measurement of signal and noise level *via* either the cell-sheet-graphene hybrid or Au mesh electrode. a) Image of experimental setups. The cell-sheet-graphene hybrid (Cell-GP hybrid) and Au mesh electrode are immersed in the PBS solution and connected to the voltage amplifier, DAQ, and computer. Then, the signal and noise levels are recorded with and without applying a 2 mV/10 Hz signal from the function generator through a separately located Pt electrode. b) Noise level measured with 0 and 10 times amplification while applying no external signal. c) Signal and noise levels measured with amplification (0, 10, 100, and 500 times) while applying a 2 mV/10 Hz signal. Quantitative data (c) of signal-to-noise ratio (S/N ratio) are acquired in quadruple (n = 4). All graphs (b,c) are the captured images from LabVIEW software.

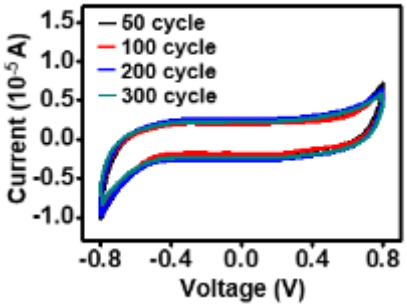

Figure S8. Measurements of charge storage capacity of Au-doped and buckled graphene mesh for 300 cycles. The area of electrode is 22.8 mm^2. The scan rate for measuring the cyclic voltammetry is 100 mV/s.

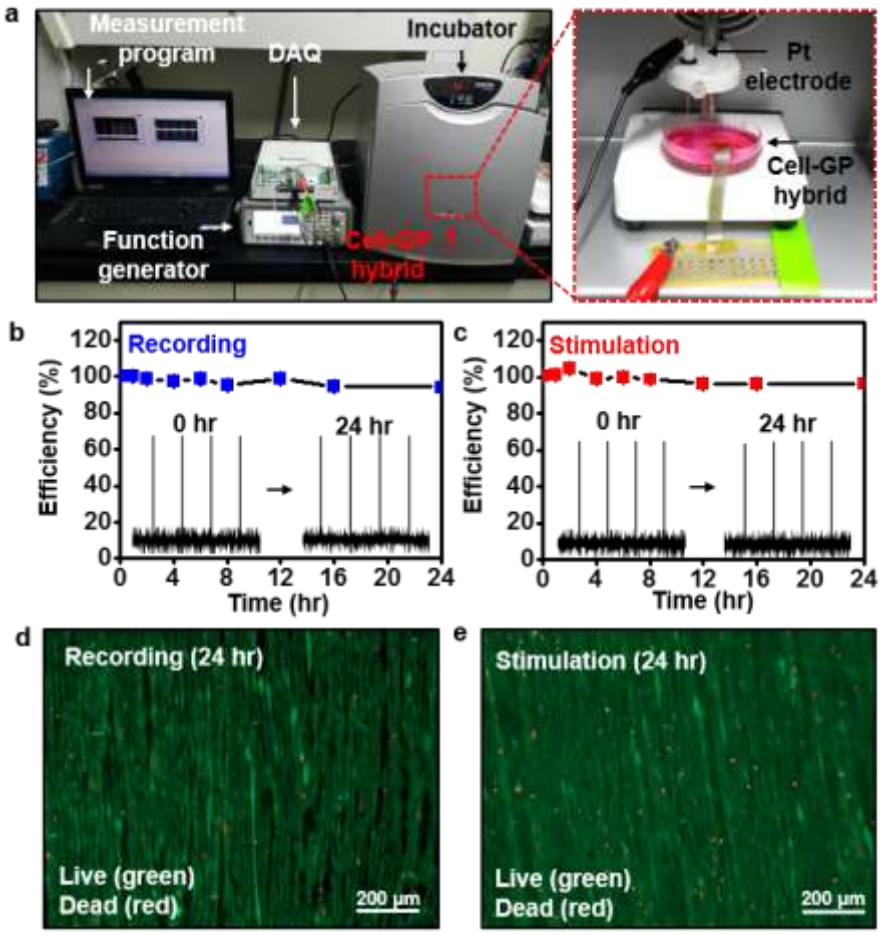

Figure S9. Investigation of cell-sheet-graphene hybrid stability under electrical stimulation/recording condition *in vitro*. a) Image of experimental setups. Each electrode (Cell-GP hybrid or Pt electrode) is connected to either function generator (1 V, 1 Hz) or DAQ accordingly depends on either recording or electrical stimulation experiments. b,c) Plots of recording (b) and electrical stimulation (c) efficiencies for the Cell-GP hybrid to investigate its electrical stability within growth medium. d,e) Fluorescence images of Live/Dead assay for the cell sheet during recording (d) and electrical stimulation (e).

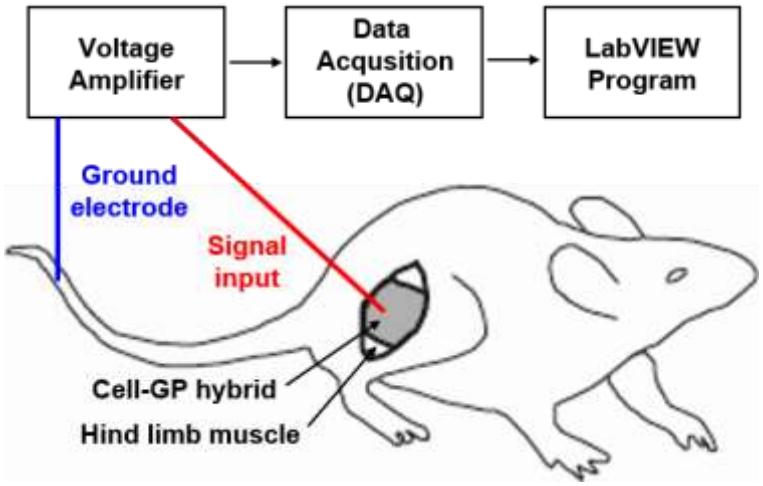

Figure S10. Schematic illustration of *in vivo* EMG monitoring experiment. EMG signal is measured *via* monopolar electrode configuration that the sensing electrode and ground electrode are mounted at hind limb muscle and a tail of mouse, respectively. The EMG signal from the muscle is passed through the voltage amplifier (×500 of gain; 10 Hz of high-pass filter and 300 Hz of low-pass filter).

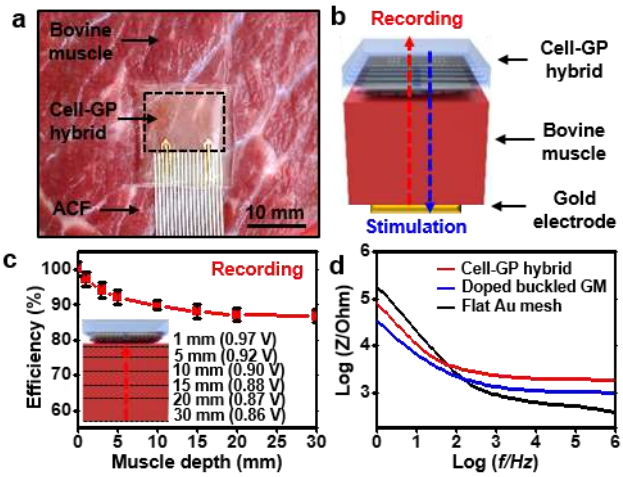

Figure S11. Characterization of the cell-sheet-graphene hybrid for recording and stimulating muscle tissue *ex vivo*. (a) Image of the hybrid implantation onto bovine muscle. (b) A schematic image of the hybrid implanted on muscle tissue *ex vivo* to ascertain the efficiency of the hybrid for its recording and electrical stimulation. The hybrid is implanted on the top of muscle, and Au electrode is placed on the bottom. (c) The efficiency for recording is decreased to ~90% as the muscle depth is increased. For recording and stimulating (Figure 6b) efficiencies, 1 V electrical signals is applied from Au electrode (hybrid for stimulating) and its signal is read at each muscle depth *via* the hybrid (Au electrode for recording). (d) Contact impedance of Cell-GP hybrid, Doped buckled GM, and Flat Au mesh.

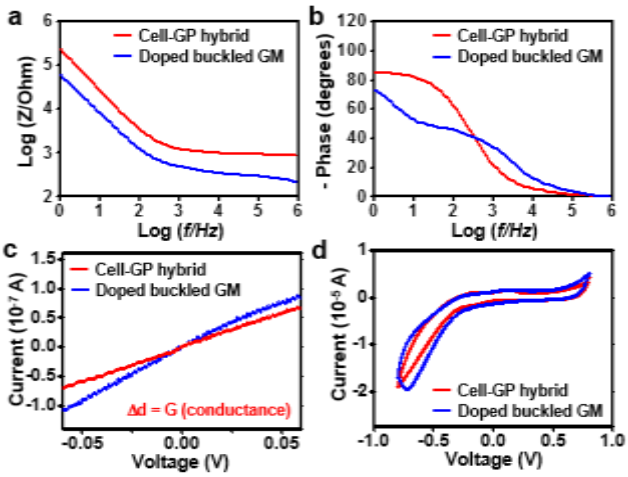

Figure S12. Electrochemical characterization of cell-sheet-graphene hybrid. a,b) Measurements of electrochemical impedance spectroscopy with impedance (a) and phase (b) plots. c,d) Measurements of conductance and charge storage capacity by plotting of I-V curves (c) and cyclic voltammograms (d). Efficiencies of Cell-GP hybrid in respect to impedance, conductance, and charge storage capacity are 81.9%, 65.6%, and 88.3% of the case without the cell layer (Doped buckled GM), respectively. All data (a-d) of cell-sheet-graphene hybrid (Cell-GP hybrid; red) and Au-doped and buckled graphene mesh (Doped buckled GM; blue) are measured in growth medium at 37 °C.

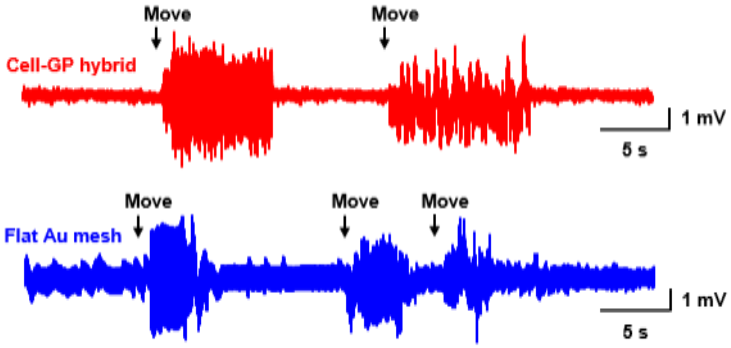

Figure S13. Measurement of the EMG signals by the cell-sheet-graphene hybrid (Cell-GP hybrid; red) and flat mesh-patterned Au electrode (Flat Au mesh; blue) during muscle contractions of the murine leg.

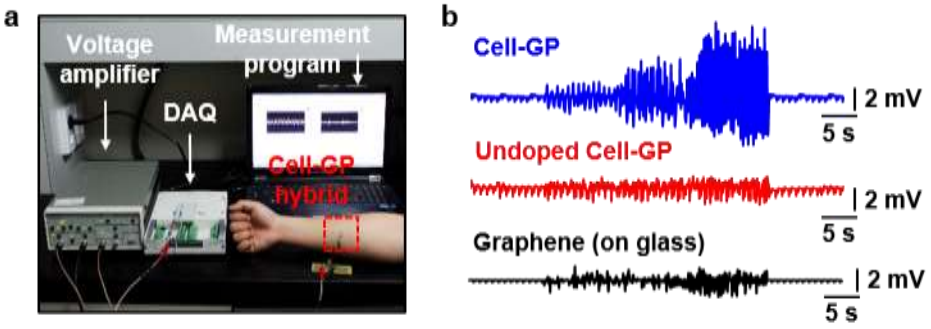

Figure S14. Characterization of EMG sensor placed on human skin. (a) Image of experimental setups for EMG sensing on human skin. The hybrid connected with voltage amplifier and DAQ is placed on human skin and its EMG signal is recorded on the program. (b) A plot of EMG signals read on human skin during small, medium, and large muscle contractions *via* cell-sheet-graphene hybrid (Cell-GP), Au-undoped and cell-sheet-graphene hybrid (Undoped Cell-GP), and graphene mesh on glass substrate (Graphene).

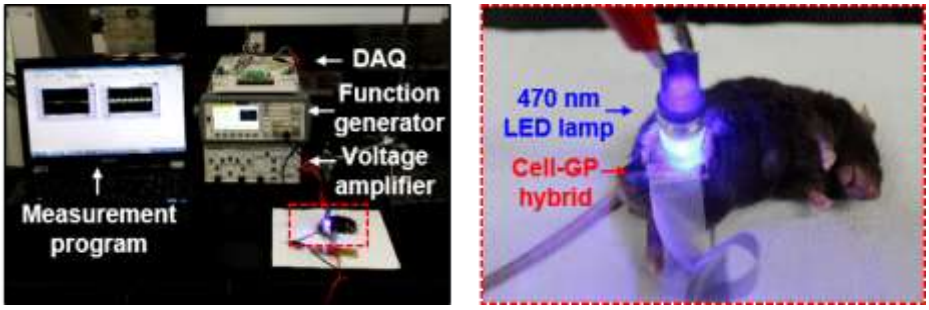

Figure S15. Images of experimental setups for the electrical/optogenetic application. EMG sensing, *via* the cell-sheet-graphene hybrid, of the hind limb muscle of channelrhodopsin 2-expressing transgenic mouse (*Thy1-ChR2*) stimulated by 470 nm blue LED placed on top of the hybrid. Optical stimulation is applied from LED lamp supplied by function generator. The EMG signal of optical-stimulated muscle contraction is processed to voltage amplifier and DAQ, and recorded through the measurement program.

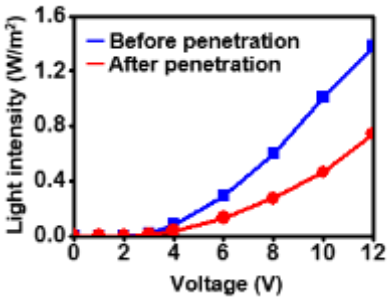

Figure S16. Light intensities of 470 nm LED lamp. Light intensities of the LED lamp as different voltages applied by function generator before and after penetration through the cell-sheet-graphene hybrid.

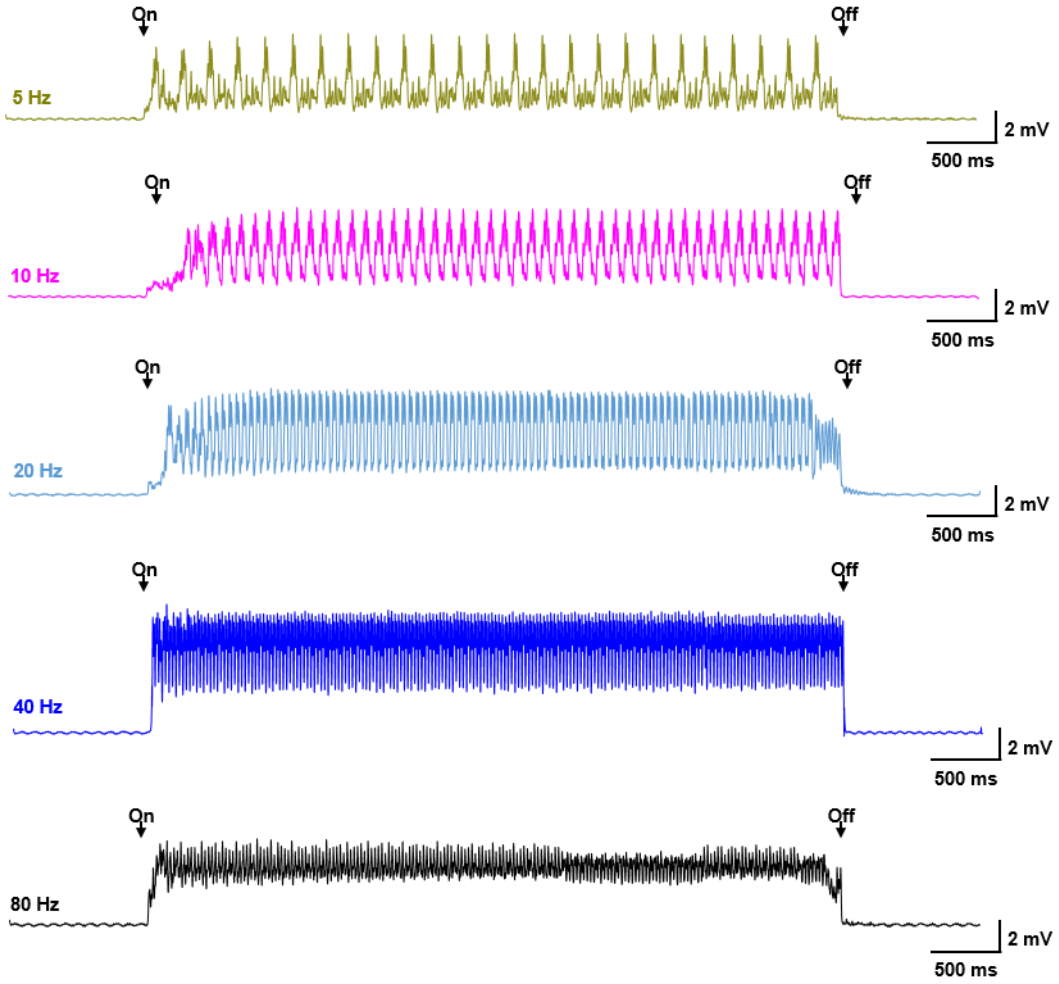

Figure S17. Filtered EMG data of cell-sheet-graphene hybrid at various frequencies of optical stimulation. Light intensity is fixed at 464 mW/m^2.

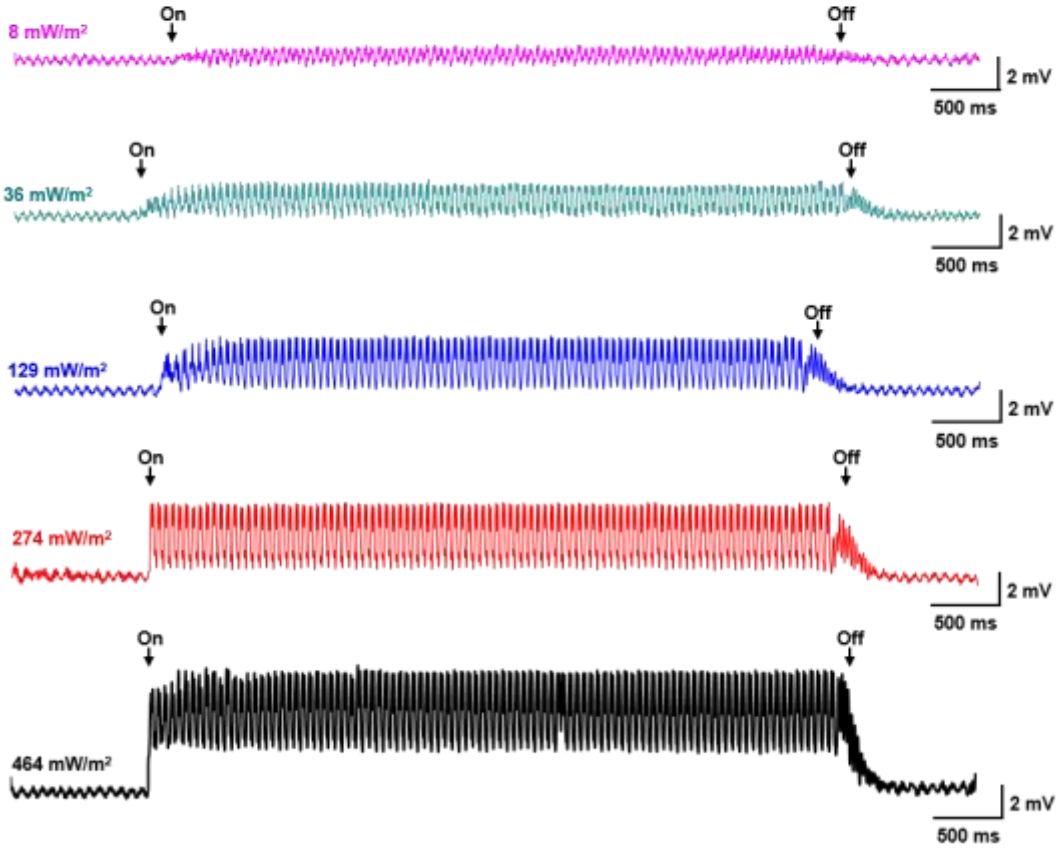

Figure S18. Filtered EMG data of cell-sheet-graphene hybrid at various light intensities of optical stimulation. Light frequency is fixed at 40 Hz.